Chapter 7 Source Time Functions

7.1 Introduction

Inverting seismic waveforms to determine the spatial and temporal rupture history of earthquakes has emerged as one of the key tools towards understanding the physics of the rupture process. Source inversions are now common for most California earthquakes larger than M6. These inversions are used to determine rupture dimensions, average slip, rupture velocity and slip heterogeneity. Unfortunately, such parameters are not systematically available for earthquakes smaller than M6. Waveform inversion requires knowledge of the response of the medium to impulses of slip in the source region (Green's functions). At periods longer than about $1s$, a layered space model can often be used to calculate Green's functions that approximate the response of the Earth. Unfortunately, it has not yet been feasible to synthesize Green's functions at periods much shorter than $1s$ — waveforms often have multiple scattered arrivals; the anelastic attenuation is unknown; and radiation patterns are commonly different from that of a double couple in a layered space. This means that it is often more difficult to resolve rupture characteristics that are shorter than $\frac{1}{2}s$ in time and $1km$ in space.

One approach to this problem is to use spectral methods (corner frequencies) to calculate source parameters. However, many of the problems just discussed are not addressed by these techniques. In many ways, most spectral techniques essentially assume homogeneous whole space Green's functions (Brune, 1970).

One solution is to utilise the waveforms of aftershocks as empirical Green's functions. This assumption is appropriate as long as —

1. the mainshock and the aftershock are co-located,

2. the mainshock and the aftershock have the same focal mechanism,

3. the source time function of the aftershock is short compared to the mainshock source time function.

A necessary (though not sufficient) condition for this assumption is that at each seismic stations, low-pass filtered displacement records from the mainshock and the aftershock are simple scalar multiples of each other. After identifying potential aftershocks by comparing locations and first motion focal mechanisms, this condition is used to identify an appropriate aftershock.

Obviously, it is also critical that the mainshock and the aftershock are well recorded at the same station. The use of aftershocks as Green's functions has only become practical with the deployment of high dynamic range seismographic networks such as SCSN. Furthermore, there must be a sufficient density of stations to obtain the azimuthal coverage that is necessary to derive directivity from the source time functions.

It is demonstrated in this Chapter that the use of aftershocks as empirical Green's Functions provides a robust method by which the directivity of moderate events can be determined. The successful inversions of the timeseries give stable source time functions at each station that are relatively insensitive to choice of aftershock as long as the aftershock approximates the location and first motion focal mechanism of the mainshock. This is promising for extending this work to invert for the rupture time history.

7.2 Theory and Methodology

The basic theory is straightforward and follows from Heaton (1982) and Hartzell and Heaton (1985):

Begin with the following definitions:

$$
\begin{aligned}
x, y &\equiv \text{Cartesian co-ordinates on the fault plane} \\
S &\equiv \text{rupture surface} \\
D(x,y,t) &\equiv \text{slip history at } (x,y) \text{ on the fault} \\
P &= \text{(average slip over fault rupture) x (rupture area)} \equiv A\overline{D} \equiv \text{potency} \\
\mu &= \text{rigidity, or shear modulus, of rock} \\
M_0 &= \text{seismic moment} \equiv \mu A\overline{D} \equiv \mu P \\
\mathbf{U}^i(t) &\equiv \text{observed vector displacement history at the } i^{th} \text{ station} \\
\mathbf{u}^i(x,y,t) &\equiv \text{vector displacement at the } i^{th} \text{ station due to the} \\
&\qquad\qquad \text{dislocation at } (x,y) \text{ on the fault} \\
\mathbf{G}^i(x,y,t) &\equiv \text{Green's functions for the } i^{th} \text{ station}
\end{aligned}
$$

Let x and y run along the fault strike and plunge, respectively. The Green's function is defined as the displacement at the receiver station due to a unit step function point dislocation at (x,y).

A schematic of the fault geometry is in Figure 7.1.

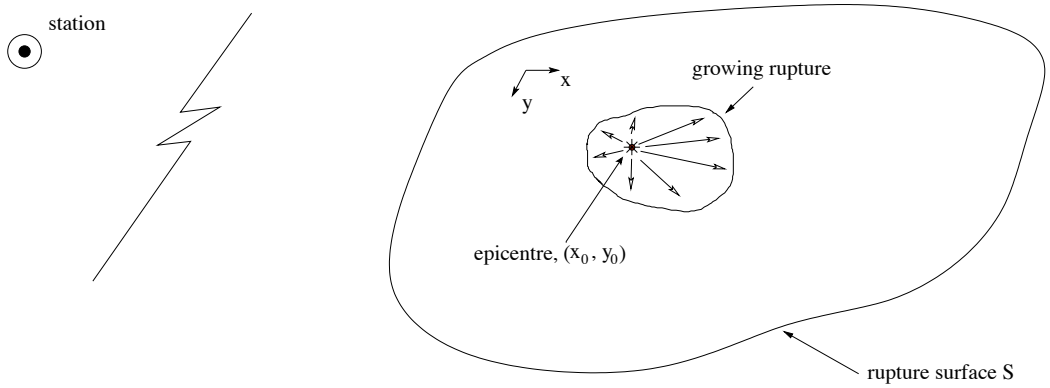

Figure 7.1: Simplified finite fault geometry for the mainshock

If a linear system is assumed, then the observed station displacement from the main-

shock is simply:

$$\mathbf{U}_M^i(t) = \iint_S \mathbf{u}^i(x,y,t)d\mathbf{S} \tag{7.1}$$

and if it is also assumed the dislocation vectors are everywhere parallel over the length of the fault (and thus the focal mechanism is invariant for all the dislocation), we may write:

$$\mathbf{U}_M^i(t) = \iint_S \dot{D}_M(x,y,t) * \mathbf{G}^i(x,y,t)d\mathbf{S} \tag{7.2}$$

where $\cdot$ and $*$ are the differentiation and convolution operators, respectively.

Now further make the assumption that over a small fault region, the Green's function at a point (x,y) is simply related to the Green's function at a single point on the fault (x_0,y_0) (in order to ensure our point is on the fault, we choose the epicentre). The Green's function will be the same but offset with a time lag $T^i(x,y)$, which is associated with the difference in travel time to the station (between the epicentre (x_0,y_0) and the point (x,y)) between key phases of the Green's functions.

$$\mathbf{G}^i(x,y,t) \approx \mathbf{G}^i(x_0,y_0,t) * \delta(t - T^i(x,y)) \tag{7.3}$$

or,

$$\mathbf{G}^i(x,y,t) \approx \mathbf{G}^i[x_0,y_0,t - T^i(x,y)] \tag{7.4}$$

This assumes that the key phases have the same apparent velocity with respect to the station as either the direct P-wave or the direct S-wave (depending on which wave group is being modelled). This is a critical approximation and it is important that individual records are investigated to ensure that we are primarily modelling wave groups with the appropriate velocity. In other words, we deconvolve the P- and S- wave trains separately. In practice, for this work, only the S-wave is deconvolved separately. The S-wave source time functions are found to be very similar to those determined from the deconvolution of the entire wave train at once.

Combining Equations 7.2 and 7.3 we obtain:

$$\mathbf{U}_M^i(t) \approx \iint_S \dot{D}_M(x,y,t) * \mathbf{G}^i(x_0,y_0,t) * \delta(t - T^i(x,y)) d\mathbf{S} \tag{7.5}$$

$$\approx \iint_S \dot{D}_M[x_0,y_0,t - T^i(x,y)] * \mathbf{G}^i(x_0,y_0,t) d\mathbf{S} \tag{7.6}$$

which can be rewritten as:

$$\mathbf{U}_M^i(t) \approx \mathbf{G}^i(x_0,y_0,t) * F_M^i(t) \tag{7.7}$$

where $F_M^i(t)$is the source time function for the i^{th} station given by:

$$F_M^i(t) \equiv \iint_S \dot{D}_M[x_0,y_0,t - T^i(x,y)] d\mathbf{S} \tag{7.8}$$

In this representation, the potency of the mainshock, P_M, is:

$$P_M \approx \int F_M^i(t) dt, \text{ for all } i \tag{7.9}$$

Now assume that the time function of the aftershock is sufficiently short so that it can be approximated by a δ-function times the potency of the aftershock, P_A, and hence:

$$\mathbf{U}_A^i(t) \approx P_A \mathbf{G}^i(x_0,y_0,t) \tag{7.10}$$

To examine the validity of this assumption, consider the definition of the moment magnitude, M_w:

$$M_w = \left[\frac{logM_0}{1.5}\right] - 10.73 \qquad , M_0 \text{ in units of dyne/cm} \tag{7.11}$$

$$\propto logM_0 \tag{7.12}$$

$$\propto log(P) \tag{7.13}$$

$$\propto log(A\bar{D}) \tag{7.14}$$

$$\propto logA^{3/2} \tag{7.15}$$

assuming a constant stress drop, and $\bar{D} \propto \sqrt{A}$:

$$M_w \propto 3/2 log A \tag{7.16}$$

so if the mainshock is an M4.5, and the aftershock being used as a Green's Function is a M2.5, then:

$$\frac{4.5}{2.5} = \frac{log(A_{4.5})}{log(A_{2.5})} \tag{7.17}$$

and so in this case the area of the mainshock is 100 times that of the aftershock. This is why the aftershock can be assumed to be a δ-function of the mainshock if they are sufficiently separated in magnitude.

Combining Equations 7.7 and 7.10 we obtain:

$$\mathbf{U}_M^i(t) \approx \left[\frac{1}{P_A}\right] \mathbf{U}_A^i(t) * F_M^i(t) \tag{7.18}$$

We can then deconvolve the aftershock motion from the mainshock motion to obtain a source time function for each station. Anyone with experience of deconvolutions of this sort will recognize that this deconvolution is typically numerically unstable. Probably the most important issue for stability is whether or not the aftershock and mainshock do indeed have similar Green's functions. This is best established by (i) ensuring that the two events are co-located and have similar first motion focal mechanisms, and by (ii) checking whether the low-pass filtered displacement records are simple scalar multiples of each other. We can then use the damped linear least squares inversion procedure to perform the deconvolution to reveal the source time function for each station. Hartzell and Heaton (1985) used a variation of this technique to derive source time functions from the teleseismic body waves of large subduction earthquakes. This formulation is similar to a serial product and is discussed by Bracewell (1965). Equation 7.18 can be rewritten in the classic form:

$$\mathbf{Ax} = \mathbf{b} \tag{7.19}$$

where in this case:

$$\mathbf{A_{jk}} = \left[\frac{1}{P_A}\right]\mathbf{U}_A^i[(j-k)\Delta t] \tag{7.20}$$

$$\mathbf{x}_j = F_M^i(j\Delta t) \tag{7.21}$$

$$\mathbf{b}_k = \mathbf{U}_M^i(k\Delta t) \tag{7.22}$$

Equation 7.19 can now be solved for the source time functions using standard linear inversion techniques. This formulation can easily be adapted to invert each component of ground motion individually, or all three components simultaneously, by a simple rewriting of the matrix equations (though inversion speeds will of course differ considerably). The method used in this Chapter is a simple least squares inversion, following Menke (1989). The deconvolution method has been discussed in detail in Chapter 1.

7.2.1 Directivity

The first-order effect we expect to see on a deconvolved source time function at a particular station is directivity. This discussion follows Heaton (2003) and ammends Lay and Wallace (1995).

The source time function can be defined as the shape of the body-wave pulses which are caused by the earthquake rupture. At distances beyond a few fault lengths, the near-field effects are dominated by far-field effects, and so only these far-field terms are considered in this case.

The far-field displacement for the P-wave, $u_r(r,t)$ (as in the radial orientation), is:

$$u_r(r,t) = \frac{1}{4\pi\rho\alpha^3}\frac{R^P}{r}\dot{M}\left(t-\frac{r}{\alpha}\right) \tag{7.23}$$

and for the SH-wave, $u_t(r,t)$ (transverse orientation), and SV-wave, $u_v(r,t)$ (vertical orien-

tation):

$$u_t(r,t) = \frac{1}{4\pi\rho\beta^3}\frac{R^{SH}}{r}\dot{M}\left(t-\frac{r}{\beta}\right) \tag{7.24}$$

$$u_v(r,t) = \frac{1}{4\pi\rho\beta^3}\frac{R^{SV}}{r}\dot{M}\left(t-\frac{r}{\beta}\right) \tag{7.25}$$

in these equations, r is distance from fault, α and β are the speed of the P- and SH/SV-waves, and R^P, R^{SH} and R^{SV} are the radiation patterns of the P-, SH- and SV- waves respectively. $\dot{M}$ is the moment rate function, the time derivative of the moment, $M = \mu A(t)\bar{D}(t)$. The radiation patterns are complex functions of the rake, strike and dip, as well as the take-off angle of the ray being considered.

For a small earthquake, the fault is considered to be single point source. As a simple approximation, displacement on this fault can be considered to occur as a ramp function. The source time function arising from a ramp time history on a single point source is a box-car of length τ_r, which is the rise time of the ramp function. For finite length faults, the rupture plane can be approximated as the summation of a number of earthquake point sources that rupture with the appropriate time delays considering the progressive rupture of the fault (see Figure 7.2). This simple line source is the Haskell Fault Model.

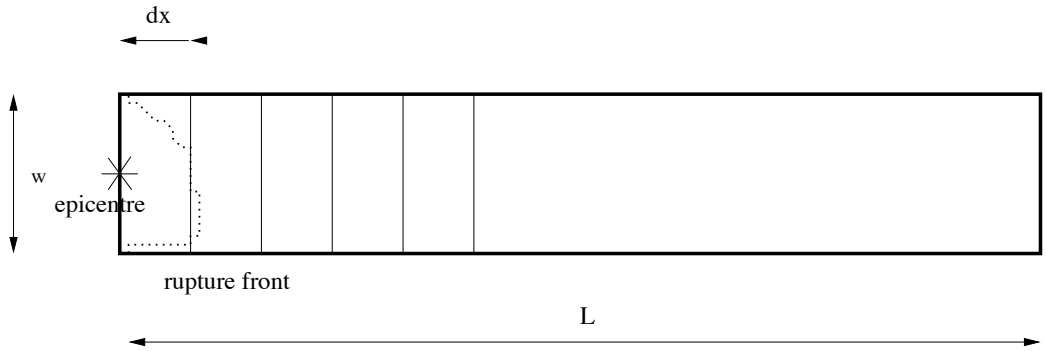

Figure 7.2: Simplified fault geometry for fault of width w and length L, with unilateral slip. Rupture plane is divided into sub-event slices of length Δx.

For the displacement field, this corresponds to:

$$u(r,t) = \sum_{i=1}^{N} u_i\left(r_i, t-\Delta t_i\right) \tag{7.26}$$

where i is an index of sub-events evenly distributed along the fault length. Δt_i is the delay time between sub-events, and if the rupture has a constant rupture velocity, v_r, and the displacement time history is the same ramp function everywhere on the fault, then $\Delta t_i = i\Delta x/v_r = x_i/v_r$. Now $\dot{M}_i$ is $\mu A_i \dot{D}_i(t)$, or $\mu w dx \dot{D}_i(t)$ if the sub-events are assumed to be over a length dx and width w. Thus, for the P-wave, combining Eqns 7.23 and 7.26 gives:

$$u_r(r,t) = \frac{\mu}{4\pi\rho\alpha^3} w \sum_{i=1}^{N} \frac{R_i^P \dot{D}_i}{r_i}(t - \Delta t_i - \frac{r_i}{\alpha})\Delta x \tag{7.27}$$

At large distance from the fault, R_i^P is approximately constant, and $r_i = r - x_i cos\theta$ (see Figure 7.3). In Equation 7.27, the r_i term in the denominator is an amplitude scaling term, and as such small changes in this denominator term will not lead to large changes in the displacements. As the length of the fault from these small events is always small in comparison to the distance of the station to the fault, the $x_i cos\theta$ term is small and aproximates zero. The r_i term in the timing cannot assumed to be constant, as the arrival times are very sensitive to these small changes in travel distances:

$$u_r(r,t) = \frac{R^P \mu}{4\pi\rho\alpha^3} \frac{w}{r} \sum_{i=1}^{N} \dot{D}\left(t - \frac{x_i}{v_r} - \frac{r - x_i cos\theta}{\alpha}\right)\Delta x \tag{7.28}$$

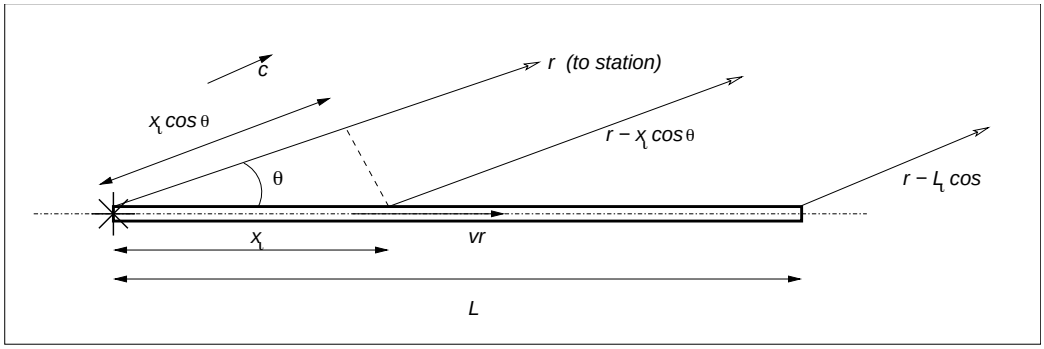

Figure 7.3: Azimuthal dependency of arrival times, for fault plane rupturing from left to right

Noting the shift property of the δ-function, and taking the limit of the sum as $\Delta x \to 0$:

$$u_r(r,t) = \frac{R^P \mu}{4\pi\rho\alpha^3} \frac{w}{r} \int_0^L \dot{D}(t) * \delta\left(t - \frac{x}{v_r} - \frac{r - x cos\theta}{\alpha}\right) dx \tag{7.29}$$

now $\dot{D}$ is independent of x and let $z = t - (x/v_r) - ([r - xcos\theta]/\alpha$:

$$u_r(r,t) = \frac{R^P \mu}{4\pi\rho\alpha^3}\frac{w}{r}\dot{D}(t) * \int_{t-r/\alpha}^{t-L/v_r-(r-Lcos\theta)/\alpha} \left[\frac{\alpha v_r}{v_r cos\theta - \alpha}\right] \delta z dz \quad (7.30)$$

$$= \frac{R^P \mu}{4\pi\rho\alpha^3}\frac{w}{r}\dot{D}(t) * \left[\frac{\alpha v_r}{v_r cos\theta - \alpha}\right] H(z)\Big|_{t-(L/v_r)-[r-Lcos\theta]/\alpha}^{t-r/\alpha} \quad (7.31)$$

$$= \frac{R^P \mu}{4\pi\rho\alpha^3}\frac{w}{r}\dot{D}(t) * B(t;\tau_c) \quad (7.32)$$

where H is the Heavyside step function, and $B(t;\tau_c)$ is a boxcar of duration τ_c ($= L/v_r + [r - Lcos\theta]/\alpha - r/\alpha$) starting at time t.

A similar form can be derived for the SV- and SH- wave displacements, using the shear wave velocity, β, and the respective radiation patterns, R^{SV} and R^{SH}.

Thus the far-field displacement source time function is determined by the convolution of 2 boxcars, one which represents the point source and the second representing the effects of the finite fault. This convolution results in a trapezoid, with duration equal to the sum of the 2 boxcar lengths, and the rise and fall of the trapezoid, equal to the duration of the shortest boxcar (see Figure 7.4).

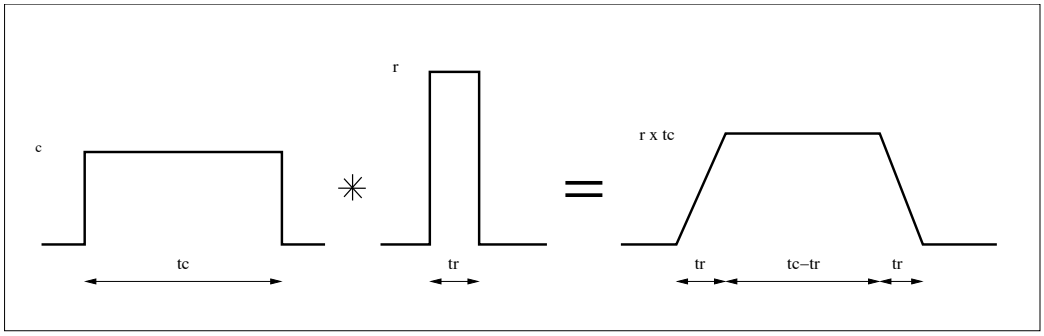

Figure 7.4: Convolution of two box-cars gives a trapezoid.

Now τ_c depends not only on the rupture speed and the fault dimensions, but also on the orientation of the observer relative to the fault. In general, the rupture speed, v_r, is less than the S-wave velocity, β. Figure 7.3 shows how the azimuth affects the arrival times — the

arrivals will reach the station from a rupture at point x at:

$$t_x = \frac{x}{v_r} + \frac{r - x cos\theta}{c} \tag{7.33}$$

and so the time τ_c, the duration of rupture for this unilateral case, as observed at the station at (r, θ), is:

$$\tau_c = \left[\frac{L}{v_r} + \frac{r - L cos\theta}{c}\right] - \frac{r}{c} \tag{7.34}$$

$$= \frac{L}{v_r} - \frac{L cos\theta}{c} \tag{7.35}$$

This is consistent with the length of the boxcar determined for the case of the P-wave, by Equation 7.32. So if a station is located along the direction of rupture propagation, $\theta = 0^o$ and τ_c is short, especially in the case of the shear wave speed ($c = \beta$), as v_r is typically $\sim 0.8\beta$. As the area under the trapezoid is constant, the amplitude will be high. A station behind the rupture propagation ($\theta = 180^o$) has a long τ_c and small amplitude. Stations located perpendicular to the rupture ($\theta = 90^o$) are not affected by the directivity.

A schematic showing how source time functions are affected by a unilaterally rupturing strike-slip fault is in Figure 7.5.

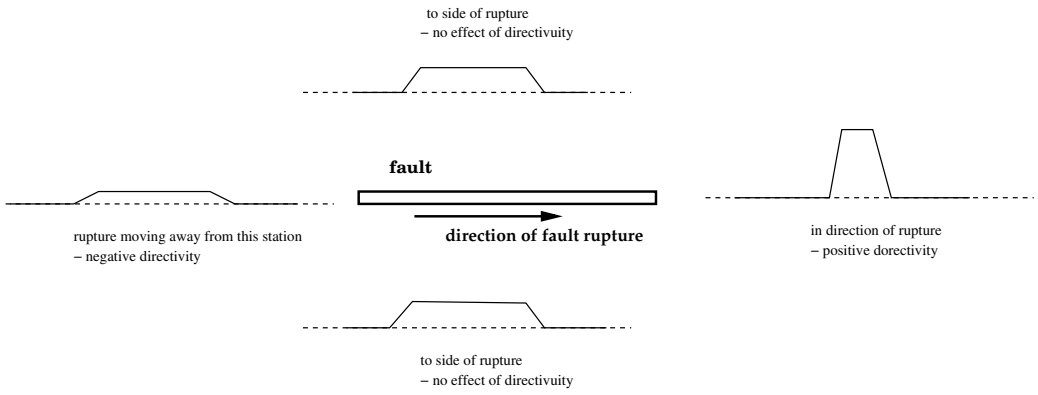

Figure 7.5: Simplified azimuthal variations for source time functions in a unilaterally strike-slip fault rupture. Note that the area under the source time function (proportional to the seismic moment, M_o) is constant, but the time, and the amplitudes, vary widely.

Observing differences in the azimuthal variation of source time functions is fundamen-

tally how we can distinguish between the real and auxiliary focal plane. Of course if the rupture is not unilateral (such as bilateral, or circular faulting), the effect of directivity will be reduced, and it will be more difficult to distinguish the true focal plane using this source time function approach.

7.3 Sample Events

In the relatively young history of the dense CISN, only a small number of earthquakes in the magnitude range of interest (M4—M6) have occurred in regions with dense high dynamic range instrumentation. Some of these earthquakes are investigated in detail. They are the 3 September 2002 M_L4.8 Yorba Linda earthquake, the 30 October 2001 M_L5.1 Anza earthquake, and the 22 Feb 2002 M_L5.4 Big Bear earthquake.

7.3.1 Yorba Linda

The M_L4.8 Yorba Linda earthquake occurred to the South East of the LA basin at 00:08:51 PDT on the 3^{rd} of September, 2002. The earthquake was accompanied by several small foreshocks (the largest a M_L2.6 at 21:50PDT the previous day), and a typical aftershock sequence (the largest a M_L2.9 at 00:15PDT). First motion analysis indicates that the earthquake was primarily strike-slip on a vertical plane striking N30^{o}W. This might be consistent with a location on the Whittier Fault. Depth was estimated to be 12.92km. First motion analysis of the aftershocks show many of these also have similar focal mechanisms and locations. Many SCSN stations are located nearby, with good azimuthal coverage. This is the ideal earthquake to test the deconvolution method.

Figure 7.6 shows the location and focal mechanism of the mainshock, and some aftershocks (as well as a foreshock) which are good candidates for use a Green's Functions as they have similar locations and focal mechanisms. Locations and focal mechanisms are from Egill Hauksson (*personal communication*).

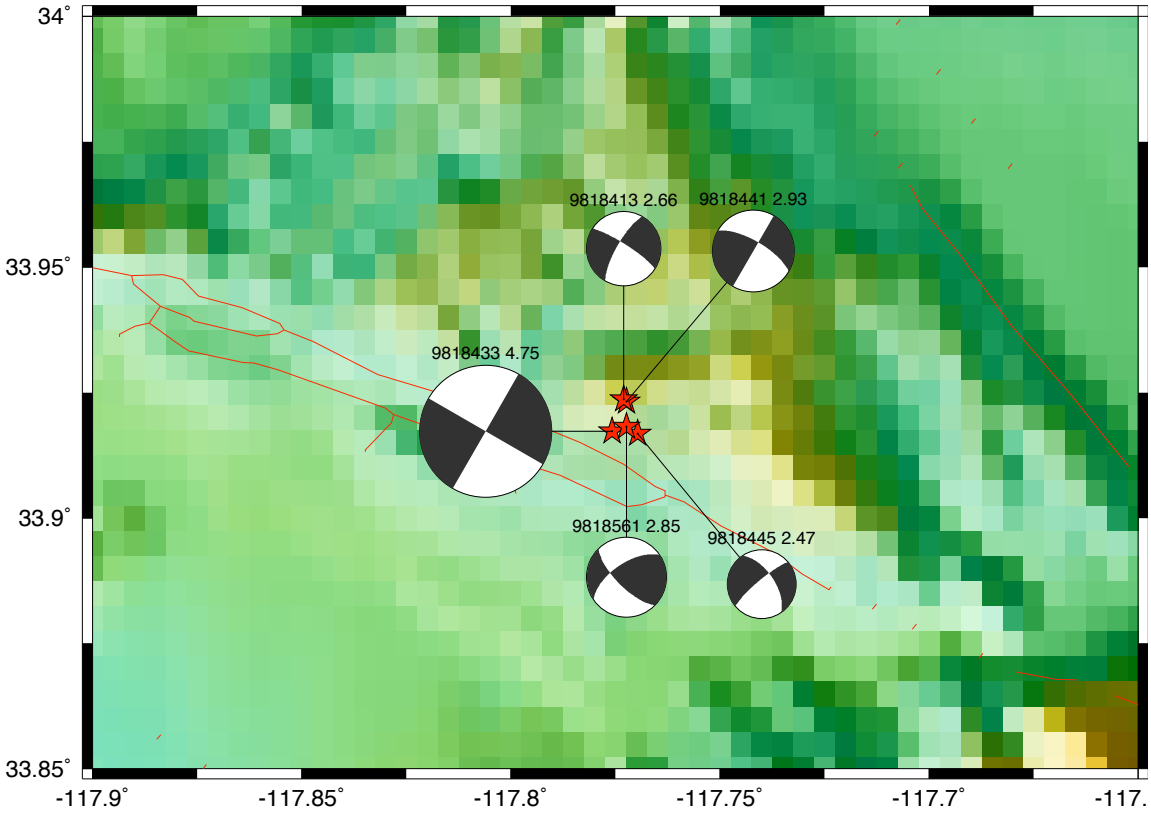

Figure 7.6: Comparison of focal mechanisms (*from Hauksson, personal comm.*) for the mainshock, a foreshock and three aftershocks in Yorba Linda sequence.

M2.85 Aftershock, 04:28:39PST 9818561, Depth = $10.27km$

Although there were other large aftershocks which occurred shortly after the mainshock, this aftershock occurred sufficiently long after the mainshock ensuring the basin waves had attenuated. First motions show the location and focal mechanisms are very similar to the mainshock. SCSN station azimuthal coverage, including all the stations that well recorded both events and are within $40km$ of the mainshock, is shown in Figure 7.7. Also on the Figure are the timeseries at each station for the components transverse to the mainshock coordinates, bandpassed between $5Hz$ and $2s$ (removing the microseismic energy which is comparable to the aftershock excitation at many stations). Even considering wave scattering, the transverse component of motion will have the highest amplitudes of SH motion, which are the waves likely to contain most information about any directivity effect for a vertical strike-slip rupture. In this Figure (as well as all subsequent Figures that display timeseries) the peak amplitude of the aftershock is scaled to the peak amplitude of the mainshock. Note the similarity of the motions, which can be better observed in Figures 7.8 and 7.9. Differences in arrival times are generally consistent with the difference in location. The deconvolution of the source time function for this component at each station is on Figure 7.9. A short duration large amplitude pulse is clearly present in stations to the NNE from the epicenter. This is consistent with the one of the focal planes as observed in the focal sphere, and is indicative of directivity in this direction.

Figures 7.11- 7.12 and 7.13- 7.14 present similar timeseries and source time functions for the radial and transverse directions. Similar directivity is obvious towards the NNE direction, even though the SH motions may not be as large for these components. Figure 7.15 compares the source time functions from all 3 components at each station, showing good repeatability from all three components at most stations.

A final investigation with this aftershock is a comparison of source time functions derived from the entire record at each station ($50s$ of data beginning with the rupture start time is used for both events), and the S-wave only (for this case, a $10s$ data segment beginning about $1s$ before the S-wave arrival is selected only). All data presented thus far has been from the whole record. Both records are tapered and padded with zeros before

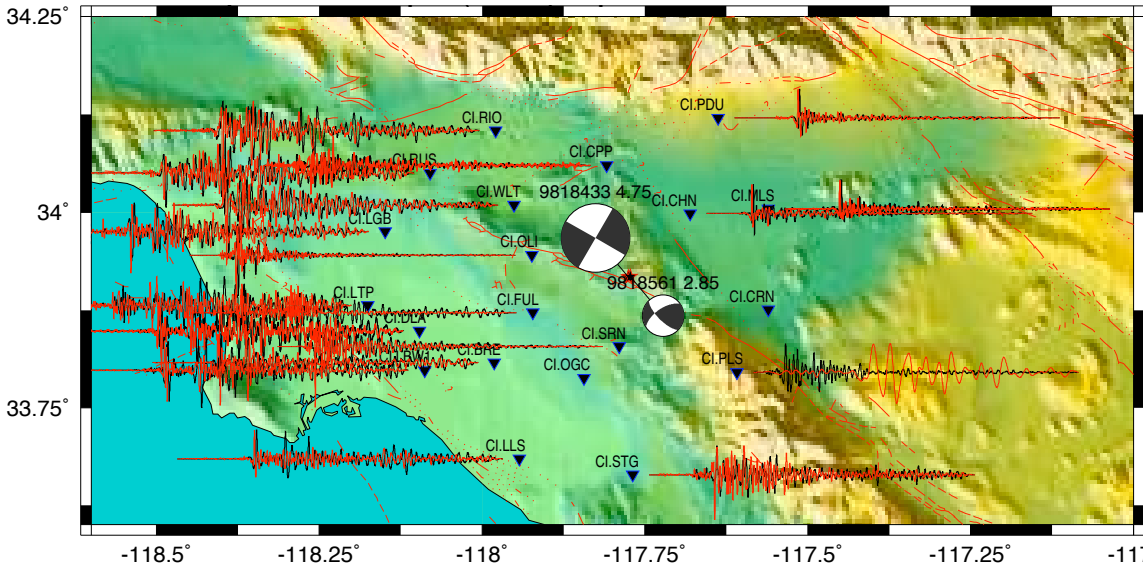

Figure 7.7: Comparison of aftershock and mainshock for Yorba Linda: Transverse component timeseries. All timeseries are scaled to the same amplitude. Black: mainshock; Red: aftershock

the inversion. Figure 7.16 shows the transverse timeseries for the S-wave only. This compares to Figure 7.8 for the entire timeseries. Figures 7.17 - 7.19 compare each component time-functions.

It is clear from these Figures there is little difference between the results of the deconvolutions using the entire tineseries and only the dominant S-wave arrivals. This is likely because the S-wave arrivals in fact dominate the response for all the components. All subsequent timeseries analysis uses data from the entire waveforms.

M2.66 Foreshock, 21:50:48PST 9818413, Depth = 13.62*km*

Figure 7.20 again shows similar timeseries shapes for the transverse components for both this foreshock and the mainshock.

Figure 7.21 shows a very similar shapes for the source time functions at most stations. Amplitude variance to other source time functions is due to difference in size of foreshock (the potency of the foreshock is not removed from the calculation).

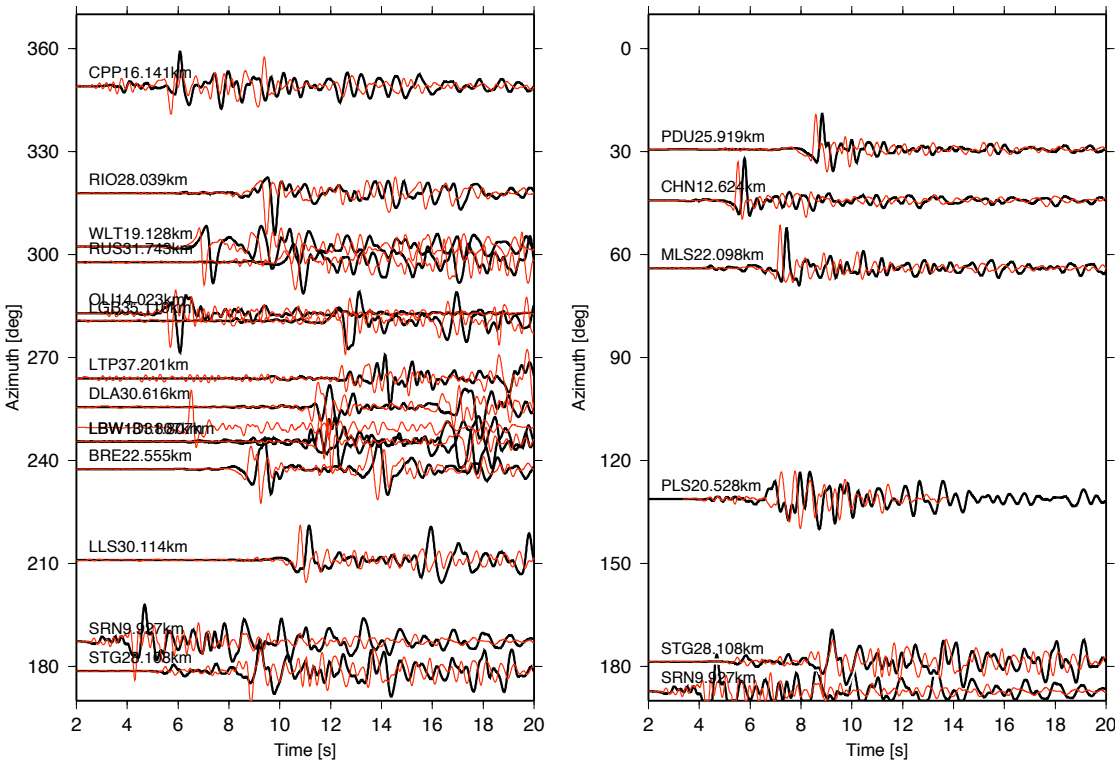

Figure 7.8: Comparison of aftershock and mainshock for Yorba Linda: Transverse component timeseries. All timeseries scaled to same amplitude. Black: mainshock; Red: aftershock

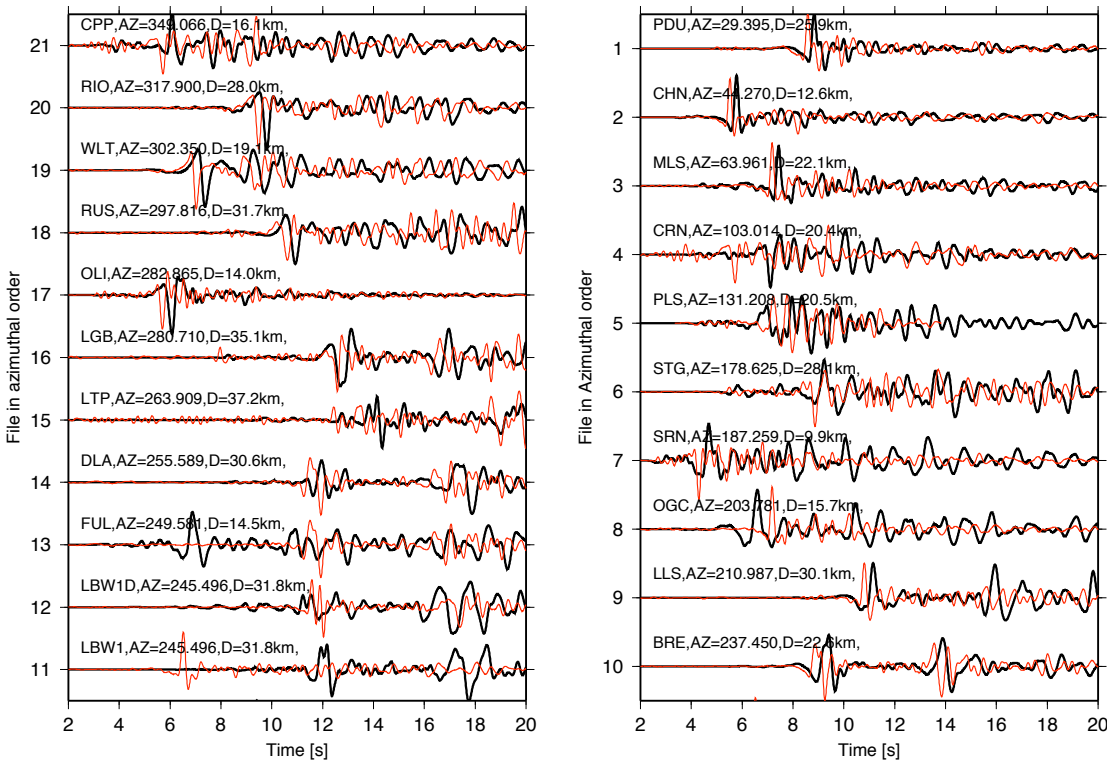

Figure 7.9: Comparison of aftershock and mainshock for Yorba Linda: Transverse component timeseries. All timeseries scaled to same amplitude. Black: mainshock; Red: aftershock

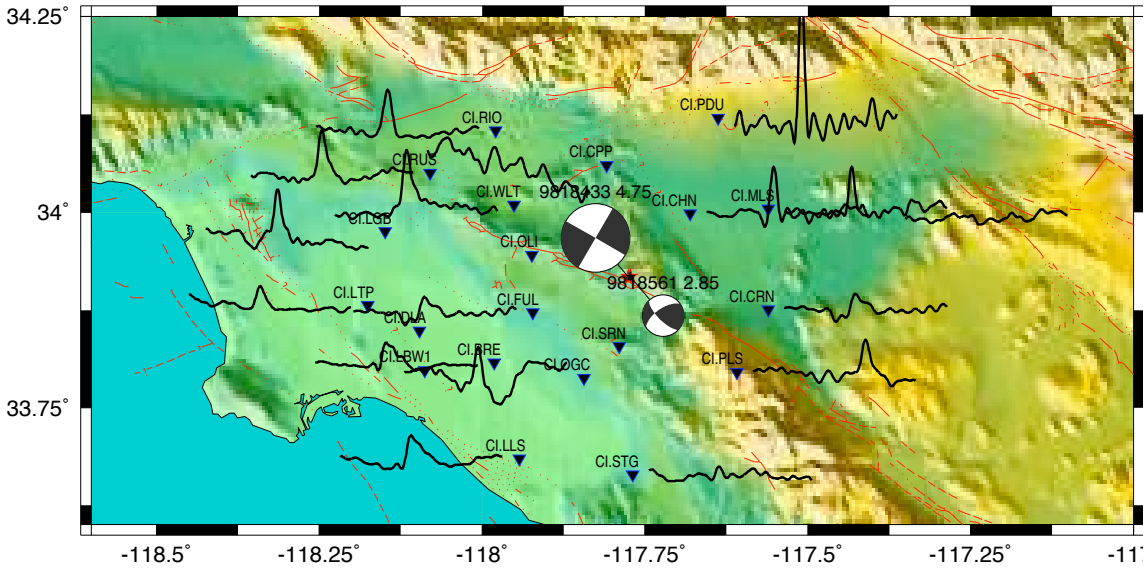

Figure 7.10: Transfer Functions for Yorba Linda from M2.85 — Transverse components. Each timeseries is 4s long, with time from $-1s$ to $+3s$. No relative scaling of amplitudes.

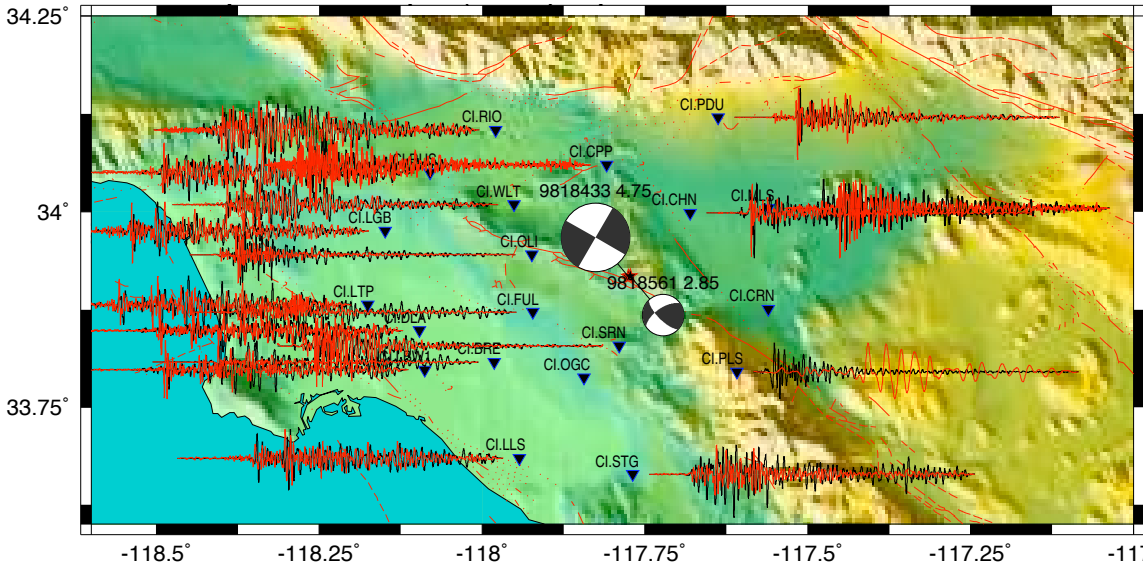

Figure 7.11: Comparison of Aftershock, Mainshock for Yorba Linda: Timeseries from M2.85 — Radial. All timeseries are scaled to same amplitude. Black: mainshock; Red: aftershock

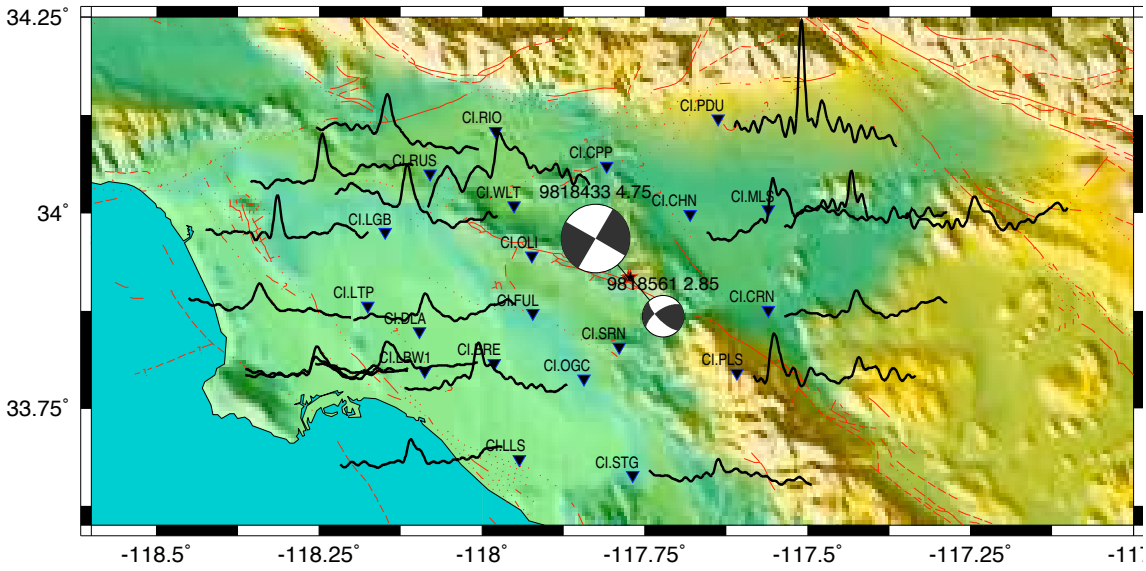

Figure 7.12: Transfer Functions for Yorba Linda from M2.85 — Radial. Each timeseries is $4s$ long, with time from $-1s$ to $+3s$. No relative scaling of amplitudes.

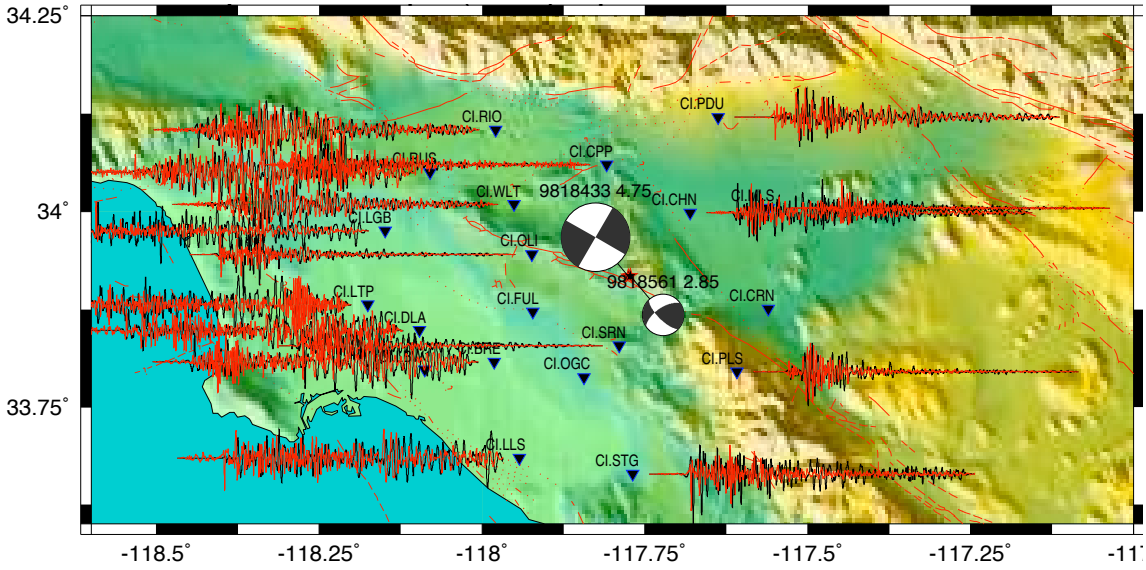

Figure 7.13: Comparison of Aftershock, Mainshock for Yorba Linda: Timeseries from M2.85 — Vertical. Black: mainshock; Red: aftershock

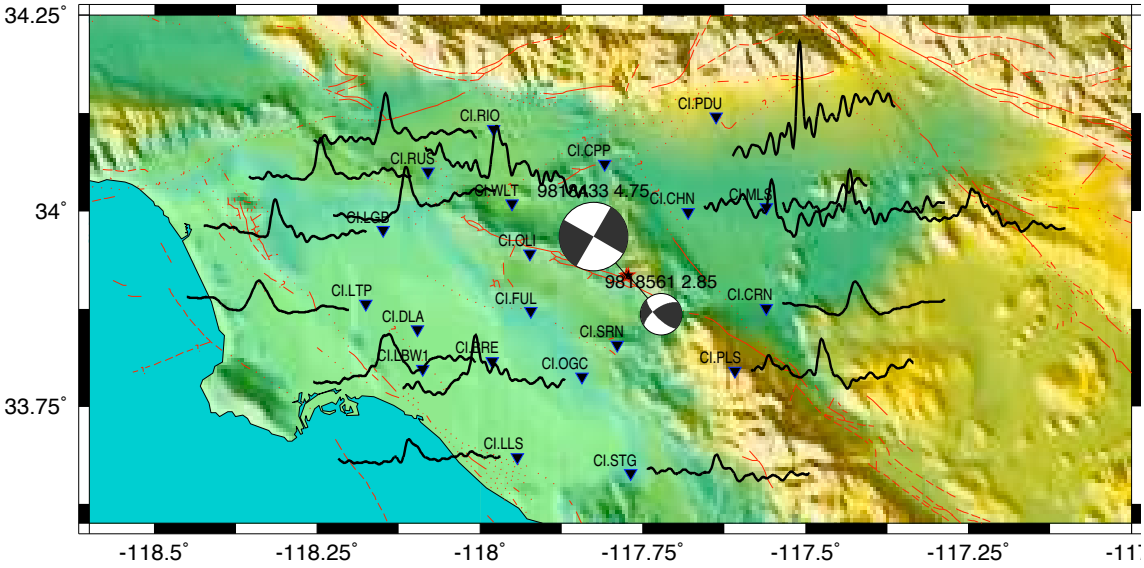

Figure 7.14: Transfer Functions for Yorba Linda from M2.85 — Vertical. Each timeseries is 4s long, with time from $-1s$ to $+3s$. No relative scaling of amplitudes.

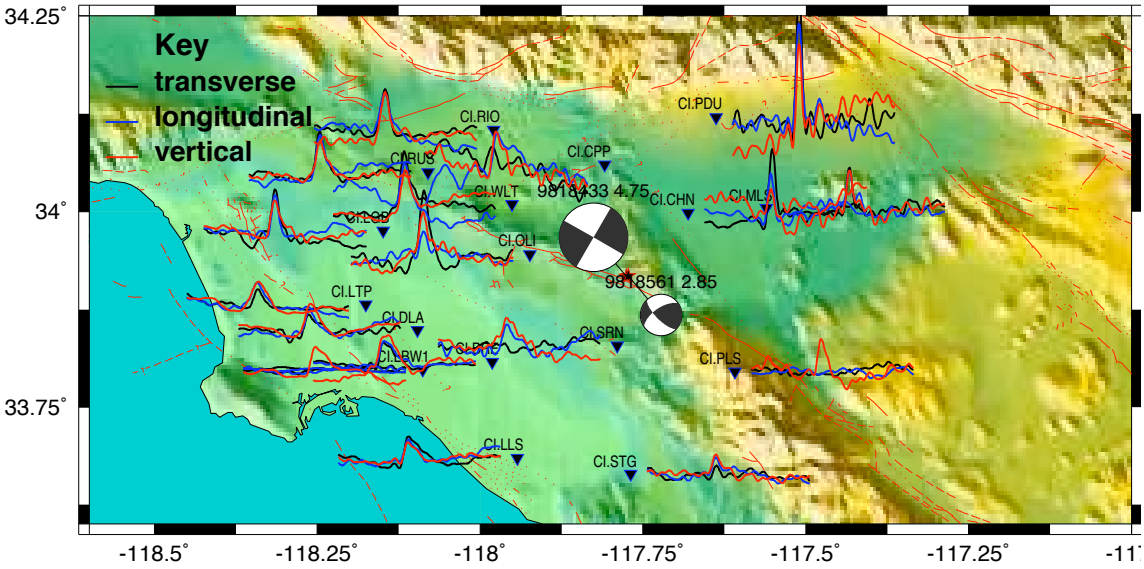

Figure 7.15: Transfer Functions for Yorba Linda from M2.85 — all components

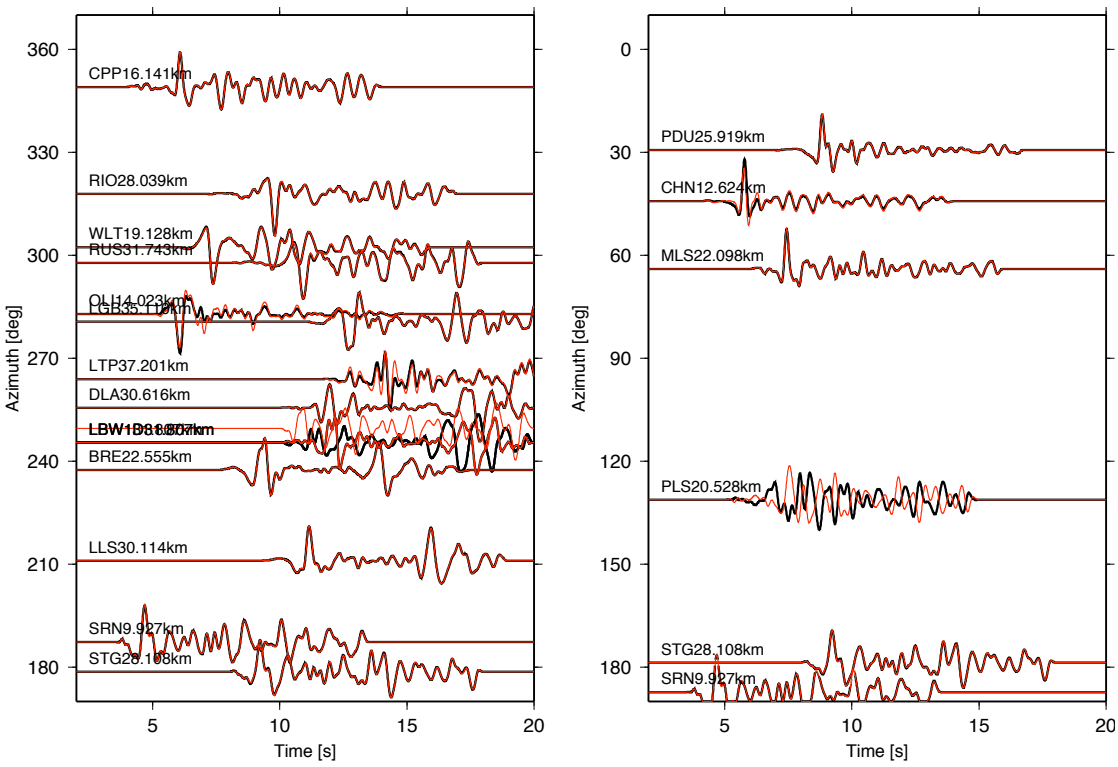

Figure 7.16: Comparison of aftershock, mainshock for Yorba Linda: Transverse S-wave timeseries. All timeseries scaled to same amplitude. Black: mainshock; red: aftershock. Compare to Figure 7.8.

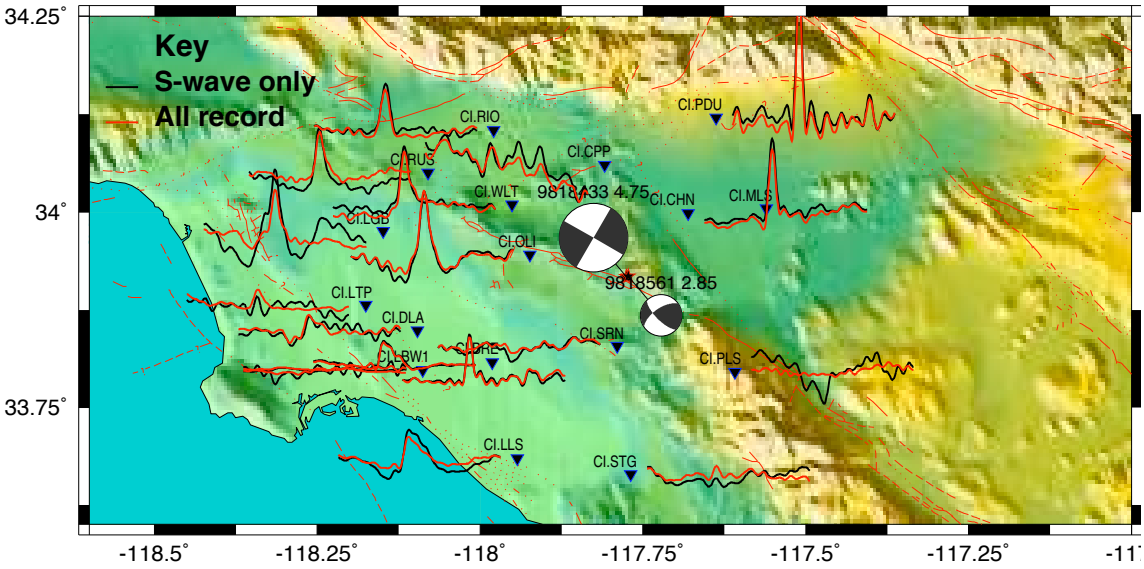

Figure 7.17: Transfer Functions for Yorba Linda from M2.85 — S-wave only vs. all waveform, Transverse components. Each timeseries is $4s$ long, with time from $-1s$ to $+3s$. No relative scaling of amplitudes.

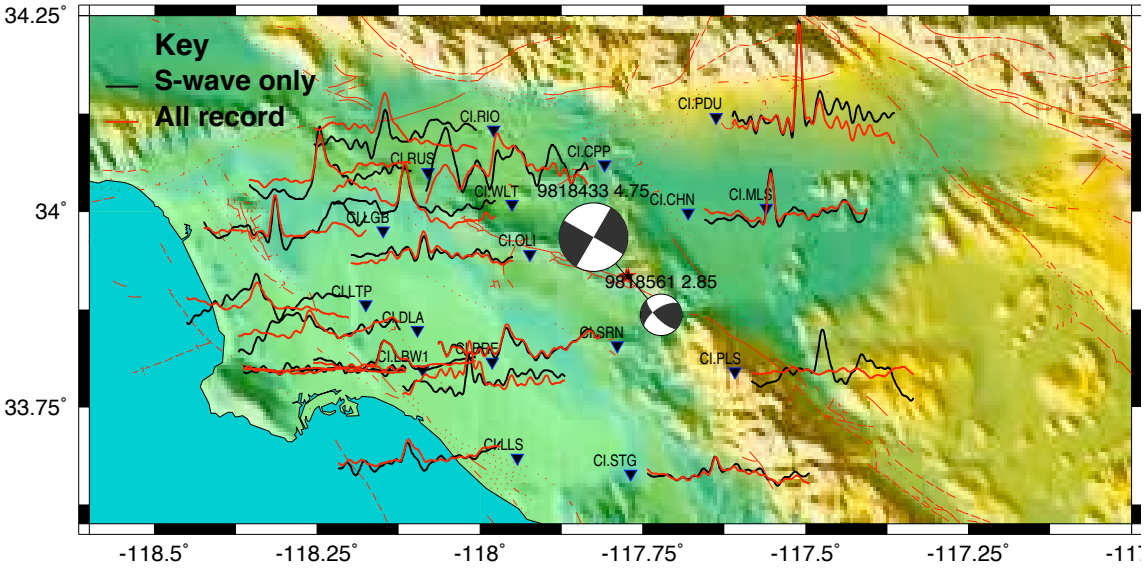

Figure 7.18: Transfer Functions for Yorba Linda from M2.85 — S-wave only vs. all waveform, Radial. Each timeseries is $4s$ long, with time from $-1s$ to $+3s$. No relative scaling of amplitudes.

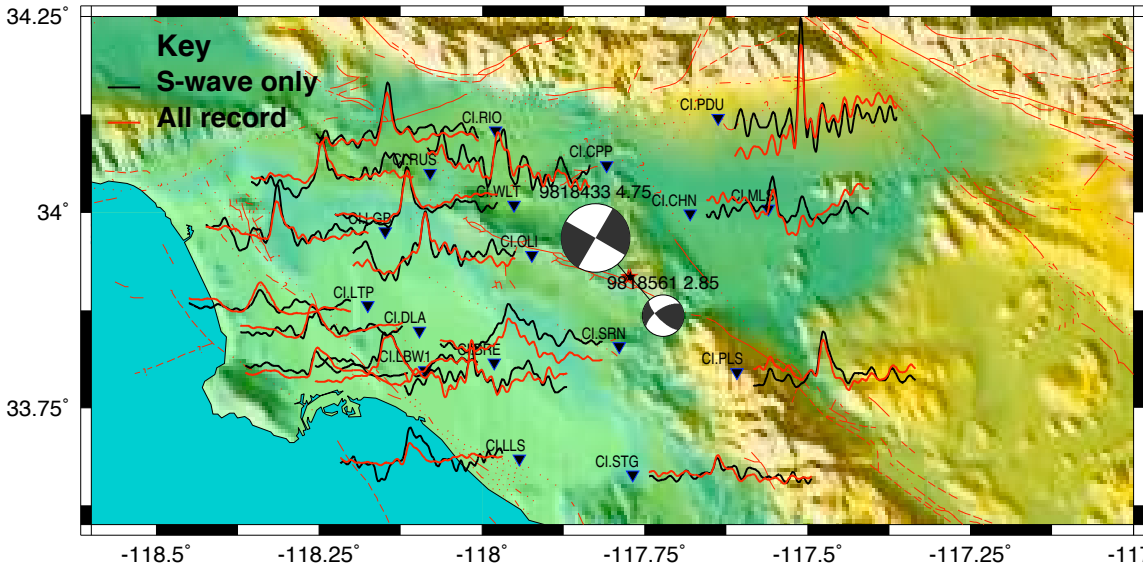

Figure 7.19: Transfer Functions for Yorba Linda from M2.85 — S-wave only vs. all waveform, Vertical. Each timeseries is 4s long, with time from $-1s$ to $+3s$. No relative scaling of amplitudes.

M2.93 Aftershock, 00:15:51PST 9818441, Depth = 11.72km

Figures 7.22 and 7.23 again show similar timeseries shapes in the transverse components for both this aftershock and the mainshock, with source time functions from all components also similar to the previous aftershock results. Amplitude variance to other source time functions is due to difference in size of aftershock (the potency of the aftershock is not removed from the calculation)

Though this earthquake occurred very soon after the mainshock (7$mins$), in the $2s-5Hz$ bandpasses used for the timeseries and thus also the source time function, the 'noise' from the mainshock is low.

M2.47 Aftershock, 00:17:09PST 9818445, Depth = 11.85km

Figure 7.24 again shows similar timeseries shapes for both this aftershock and the mainshock. This M2.47 event occurred just 78s after a M2.93 aftershock discussed previously, and so the smaller motions generated by this event are somewhat swamped by the coda from the previous aftershock. This is very clear in the stations to the west of the epicenter,

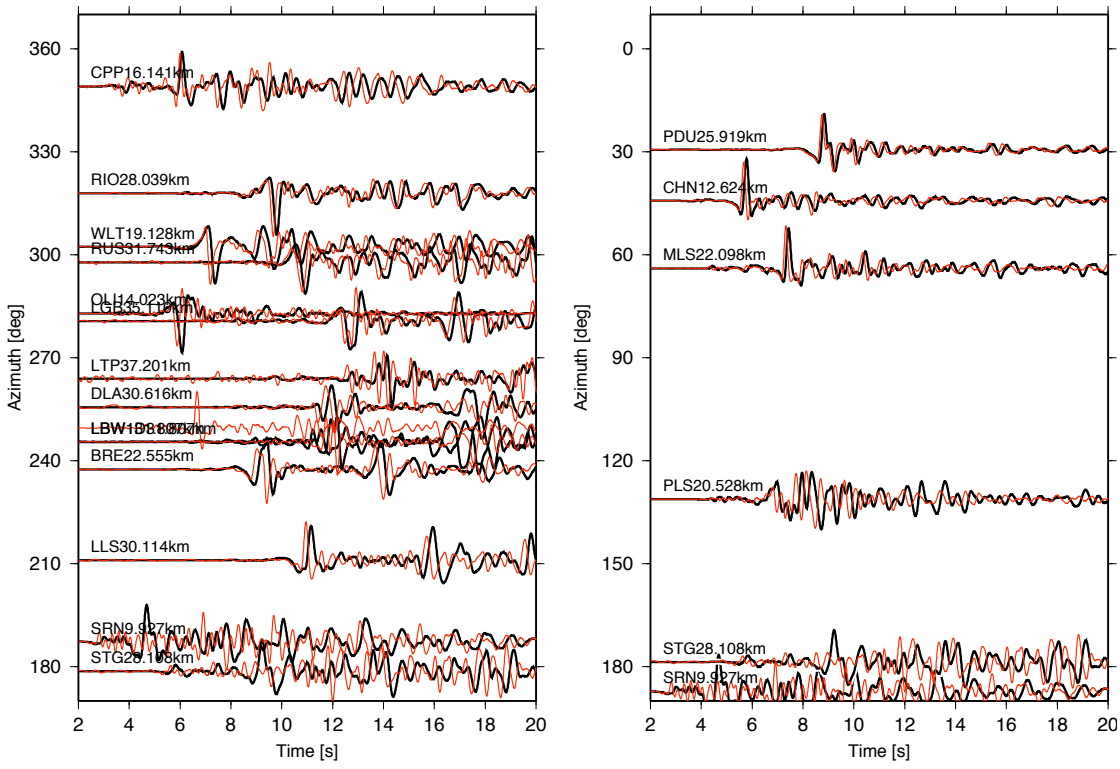

Figure 7.20: Displacement timeseries comparison with M2.66 and mainshock — Transverse component. Black: mainshock; red: aftershock

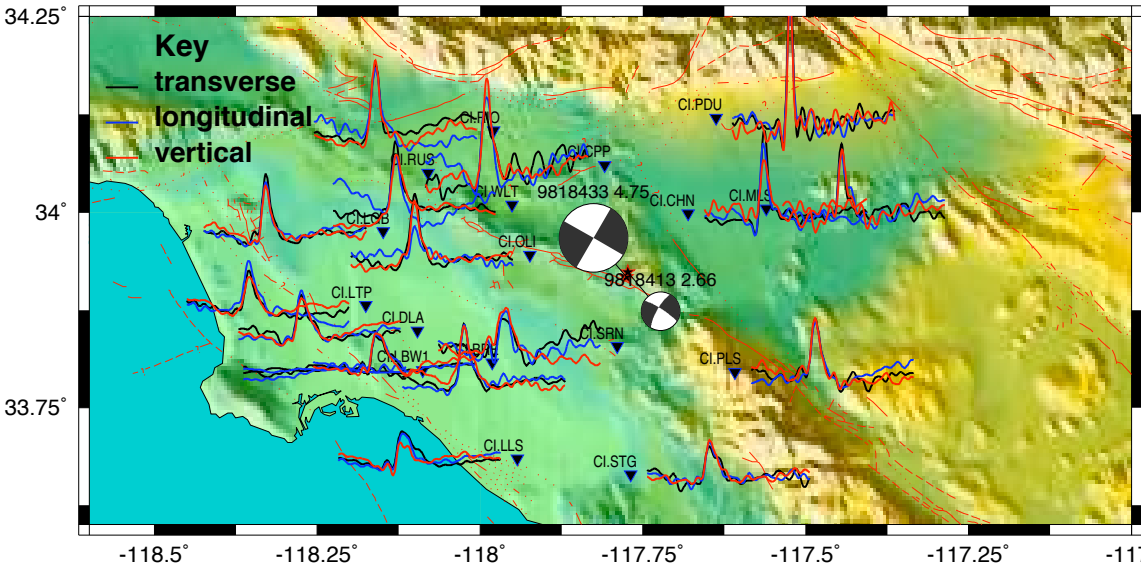

Figure 7.21: Transfer Functions for Yorba Linda from M2.66 — all components. Each timeseries is $4s$ long, with time from $-1s$ to $+3s$. No relative scaling of amplitudes.

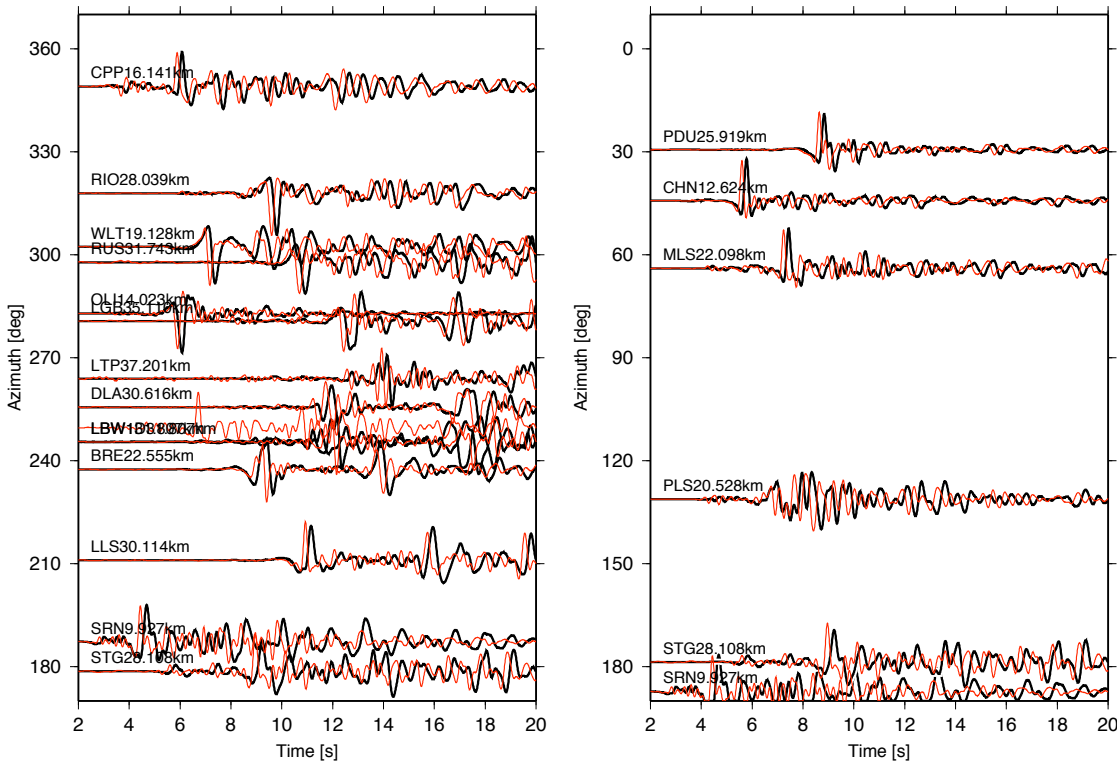

Figure 7.22: Displacement timeseries comparison with M2.93 and mainshock — Transverse component. Black: mainshock; red: aftershock

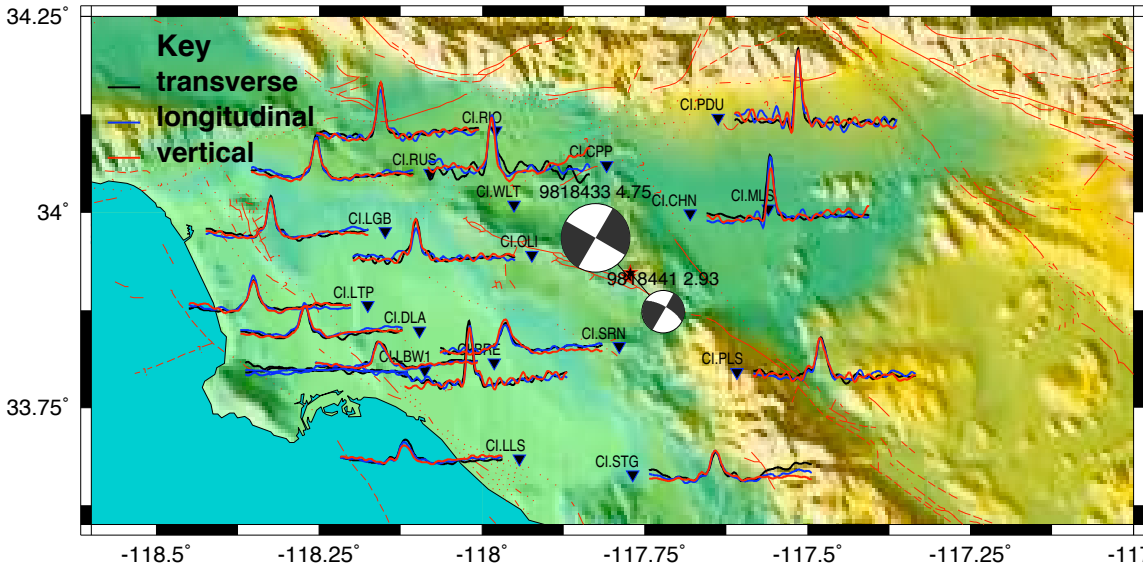

Figure 7.23: Transfer Functions for Yorba Linda from M2.93 — all components. Each timeseries is $4s$ long, with time from $-1s$ to $+3s$. No relative scaling of amplitudes.

which are predominantly basin sites. The rock sites to the east do not appear to have this effect.

Figure 7.25 shows a much poorer source time function for most stations, with a very noisy timeseries. This is likely due to the residual basin waves from the M2.93 event, that are not attenuated, and are of similar order of magnitude to the M2.47 body wave magnitudes. This event is the smallest investigated, and all the source time function map figures employ the same scaling, which explains the larger amplitudes of the source time functions in this Figure. The potency is not removed from these plots.

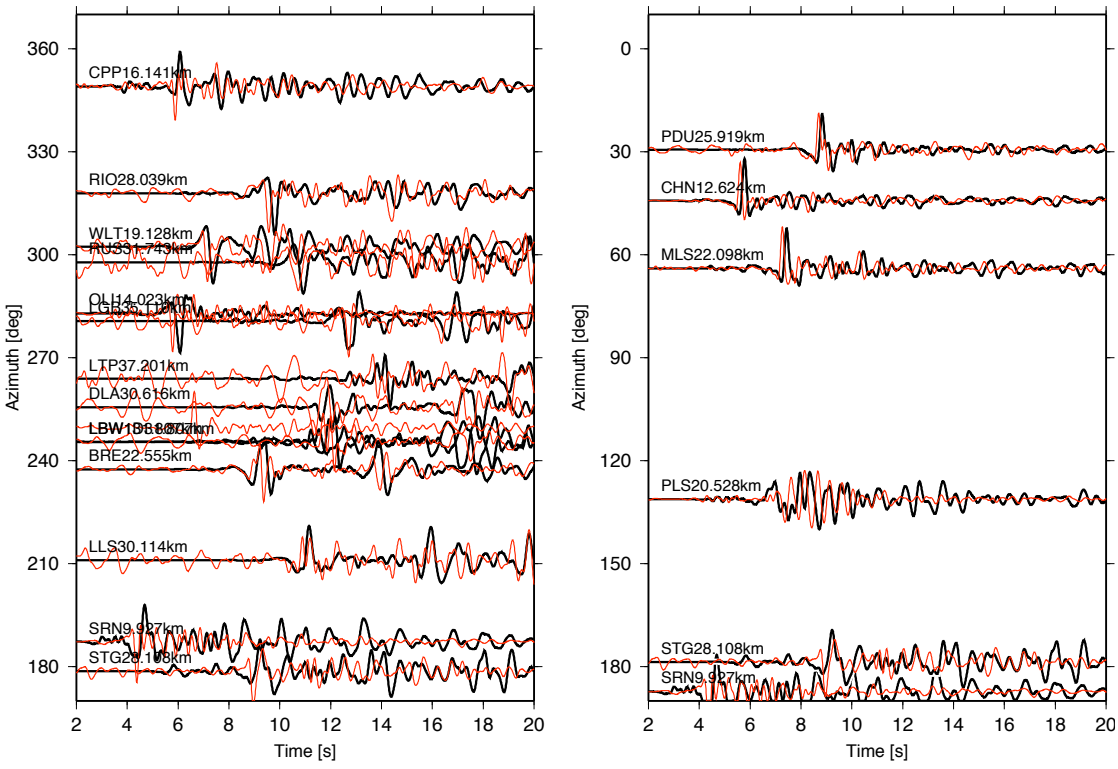

Figure 7.24: displacement timeseries comparison with M2.47 and mainshock — Transverse component

In general, it appears the accuracy of the method is relatively insensitive to the choice of aftershock, as long as the focal mechanisms, locations, and depths are similar. Signal to noise should also be good for the foreshock to minimise noise in the resulting source time functions, which is shown to be problematic if events are small and occur shortly after

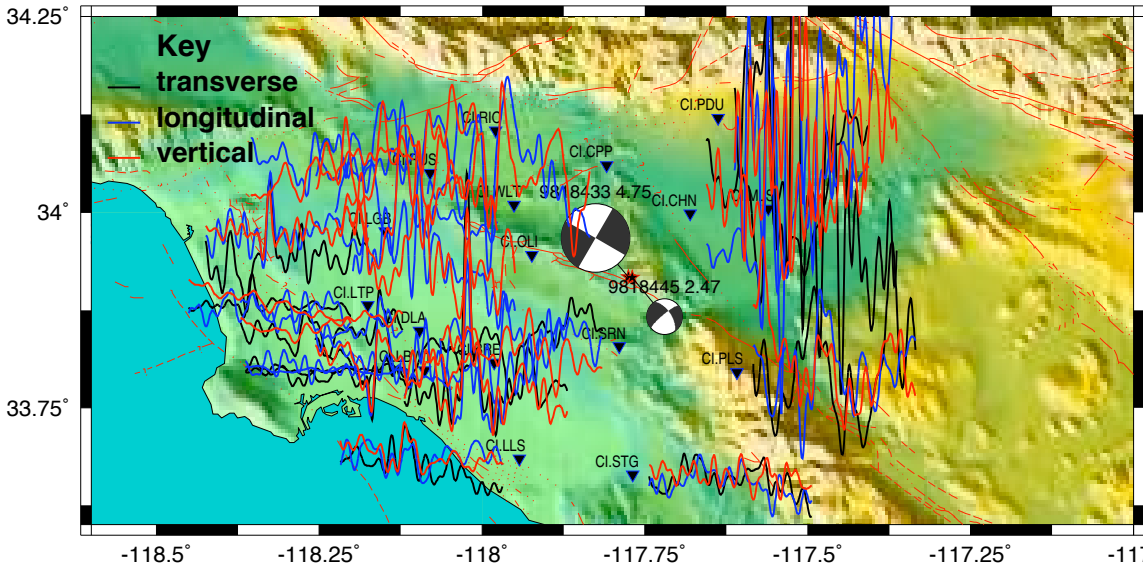

Figure 7.25: Transfer Functions for Yorba Linda from M2.47 — all components

larger events.

Figures 7.26 and 7.27 compare the timeseries and time-functions from all aftershocks at the stations in the apparent forward directivity direction (PDU), to the sides (WLT, PLS) and behind the directivity pulse (PLS). Magnitudes are as expected, with larger amplitudes for source time functions derived from smaller magnitude aftershocks. Time offsets can be explained by the small differences in locations between all the events. The strange timing and amplitude at Station PLS for the M2.85 aftershock is likely a data processing/archiving problem rather than a true reflection of the data. Ignoring the smallest aftershock, which had problems with signal-to-noise, there is significant similarity in all the 'Green's Functions' for the differing aftershocks. These results are very similar to the simplified theoretical solution shown in Figure 7.5. Figure 7.28 presents the same data as Figure 7.27, but has the amplitudes scaled by their potency, relative to the M2.93, which is determined from the magnitudes, following Equations 7.15 and 7.17.

7.3.2 Big Bear

A M_L5.4 earthquake struck the region of Big Bear Lake on the 22^{nd} of February, 2002, at 04:19PST. Depth was estimated to be 1.23km. The event was located 5km north of

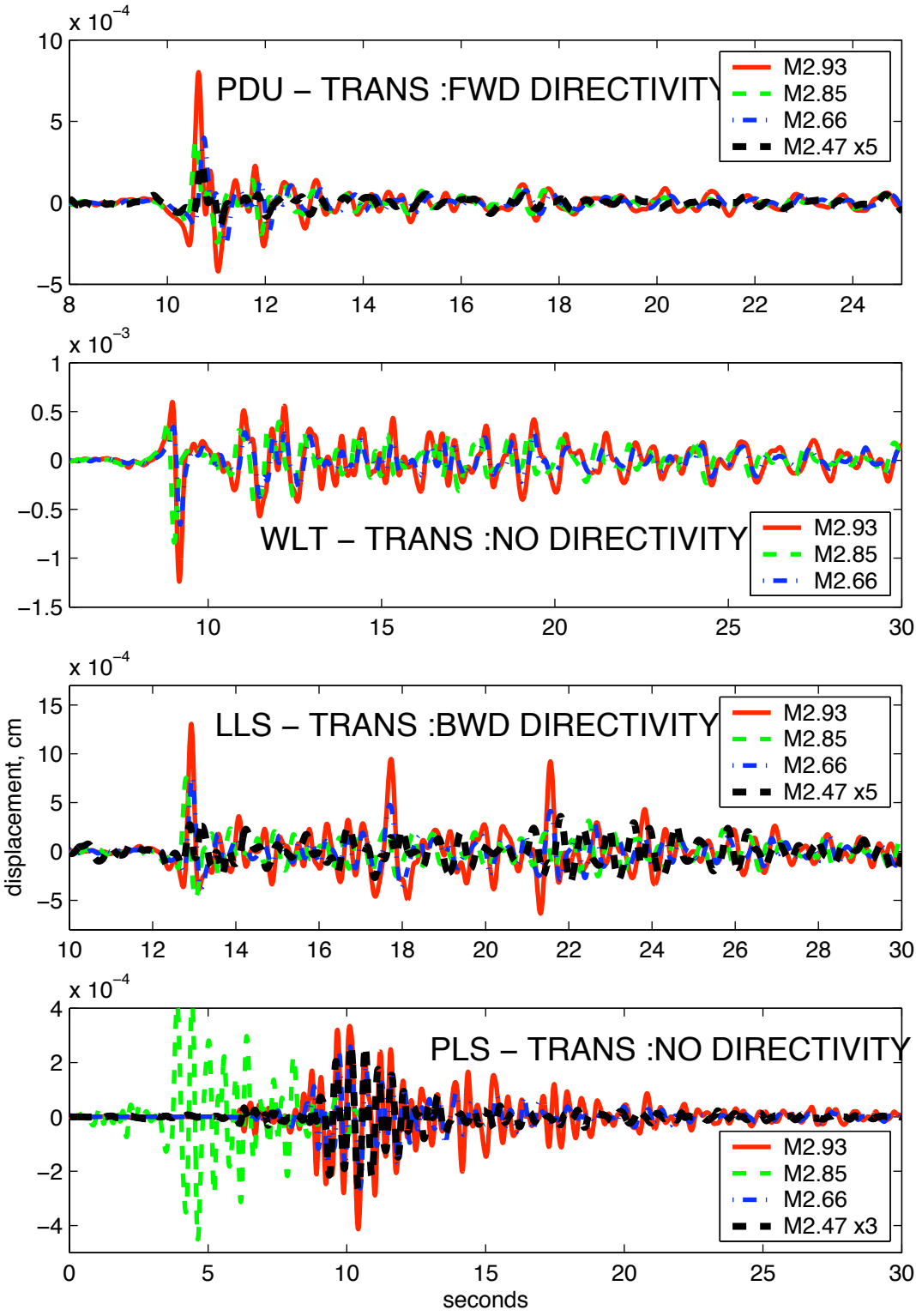

Figure 7.26: Yorba Linda: individual station timeseries comparison.

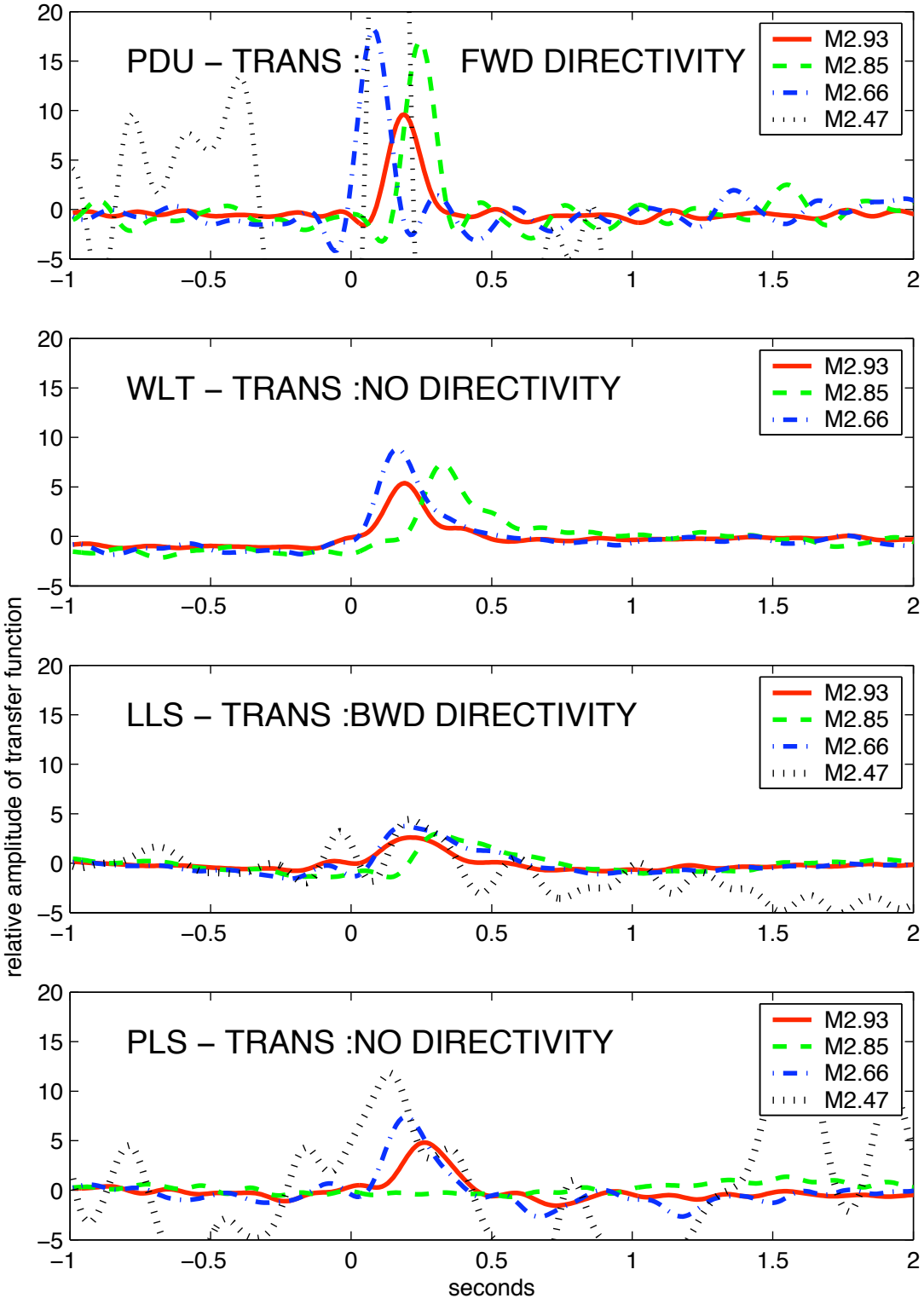

Figure 7.27: Yorba Linda: individual station source time series comparison.

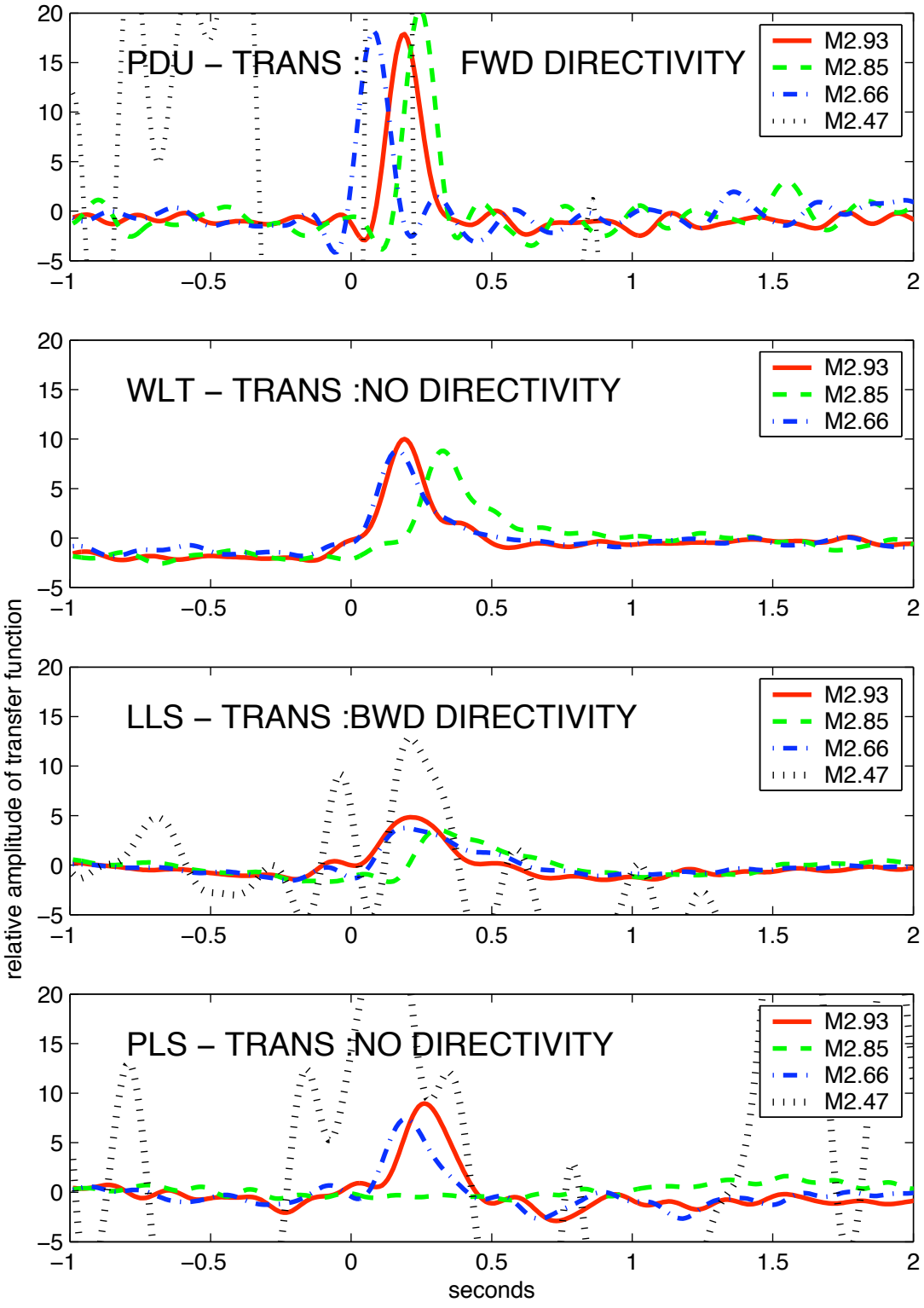

Figure 7.28: Yorba Linda: individual station source time series comparison. All events are scaled by potency, relative to M2.93 event.

Big Bear and thus north of the aftershock zone of the 1992 Big Bear earthquake (M6.2). The mainshock exhibited strike-slip faulting (horizontal movement) on a steeply dipping (80^o) plane striking N40^{o}W, sub-parallel to the local strike of the Helendale fault. This mechanism is consistent with the mainshock being near the Helendale fault.

Figure 7.29 presents the focal mechanism of the mainshocks and some selected aftershocks. Locations and focal mechanisms are again from Egill Hauksson (*personal communication*).

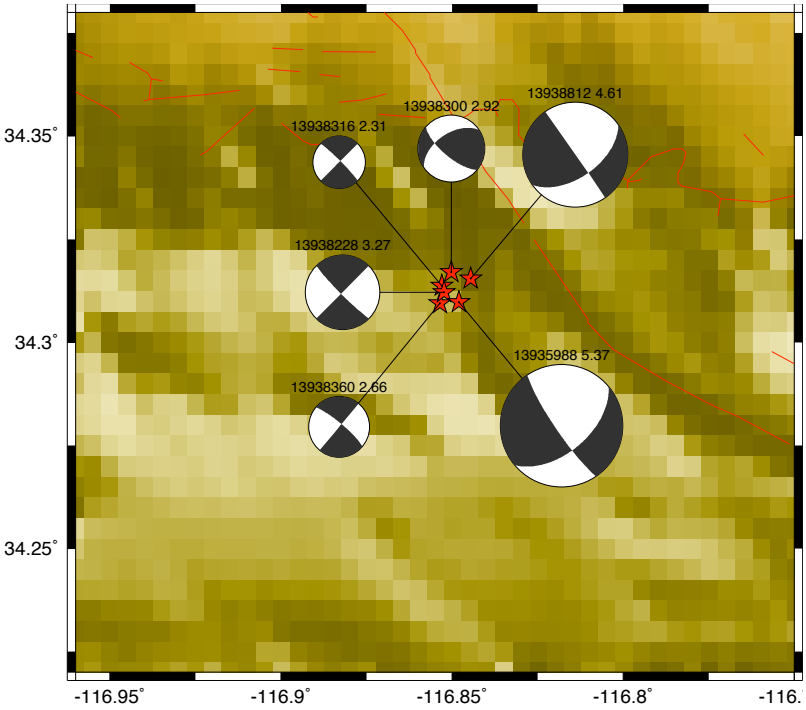

Figure 7.29: Comparison of focal mechanisms (*from Hauksson, personal comm.*) for the mainshock, a foreshock and three aftershocks in Big Bear sequence.

The aftershocks investigated all occurred at least 15 hours after the mainshock, and range in size from M$_L$2.31 to M$_L$4.61. They are:

1. M$_L$3.27, 20:03:59PST (23Feb2004) 13938228, Depth = 6.16km
2. M$_L$2.92, 00:27:00PST (24Feb2004) 13938300, Depth = 4.62km
3. M$_L$2.31, 01:31:07PST (24Feb2004) 13938316, Depth = 6.11km
4. M$_L$2.66, 04:15:39PST (24Feb2004) 13938360, Depth = 5.84km
5. M$_L$4.61, 20:03:04PST (25Feb2004) 13938812, Depth = 2.71km

Figures 7.30–7.34 show the source time functions as determined for the three components. The station density is not as good as observed in the Yorba Linda earthquake, especially to the North and East, where the desert and San Bernadino mountains lie respectively. Nonetheless, there does appear to be directivity to the North-East.

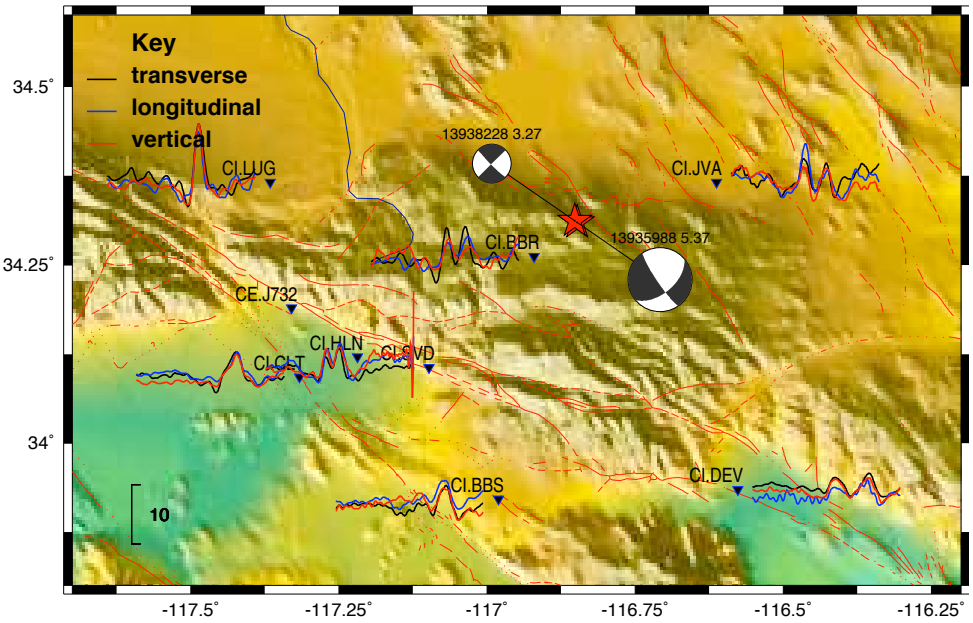

Figure 7.30: Transfer Functions for Big Bear from M3.27 — all components. Each timeseries is $4s$ long, with time from $-1s$ to $+3s$. Black: mainshock; red: aftershock

From the shape of the source time functions, it appears most likely the rupture plane is the NE-SW trending plane. This is inconsistent with the nearby Helendale fault. Directivity is towards the North-West. Figure 7.35 presents comparisons of the source time functions for stations approximately in the line of directivity (LUG), behind the rupture front (DEV) and to the sides (JVA, SVD). Figure 7.36 shows the displacement time series from these stations. Due to the very wide variability in amplitude, all timeseries are scaled to unit amplitude.

7.3.3 Anza

A M_L5.1 earthquake occurred at 23:56PST, on the 30^{th} of October, 2001, 10 miles southeast of the town of Anza in northern San Diego County. It was located within the 5 km wide

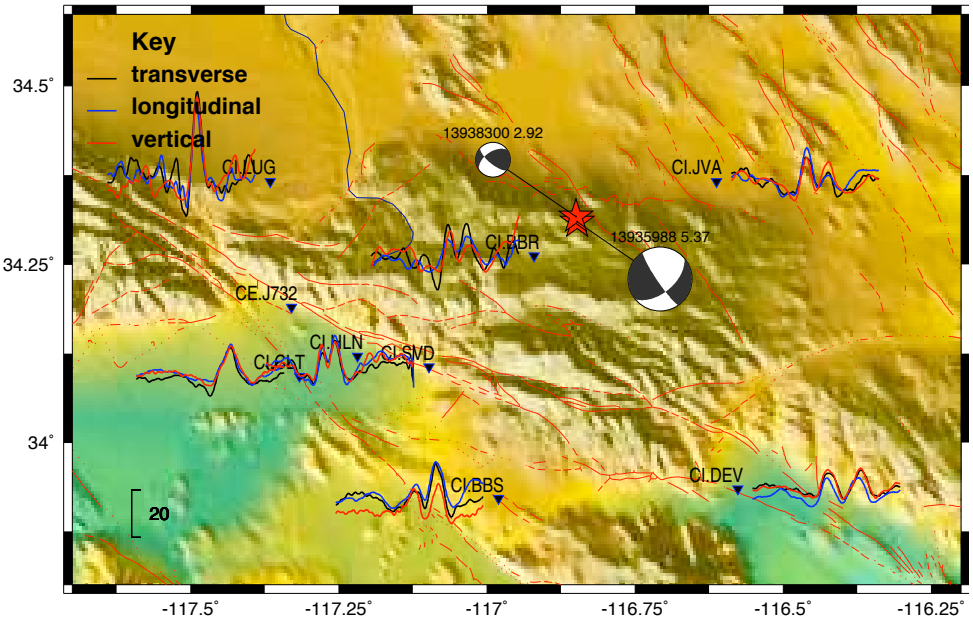

Figure 7.31: Transfer Functions for Big Bear from M2.92 — all components. Each time-series is $4s$ long, with time from $-1s$ to $+3s$.

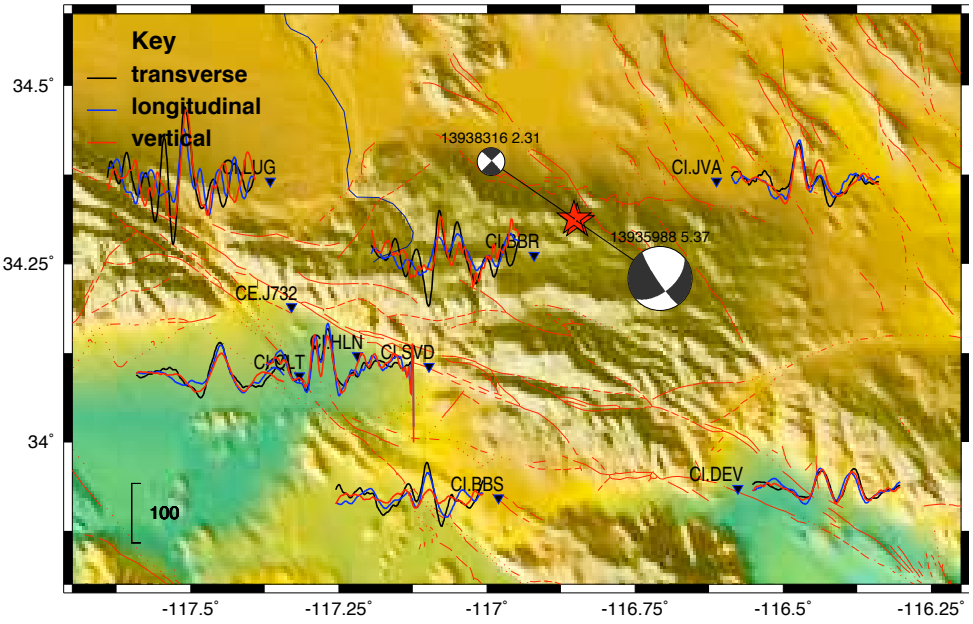

Figure 7.32: Transfer Functions for Big Bear from M2.31 — all components. Each time-series is $4s$ long, with time from $-1s$ to $+3s$.

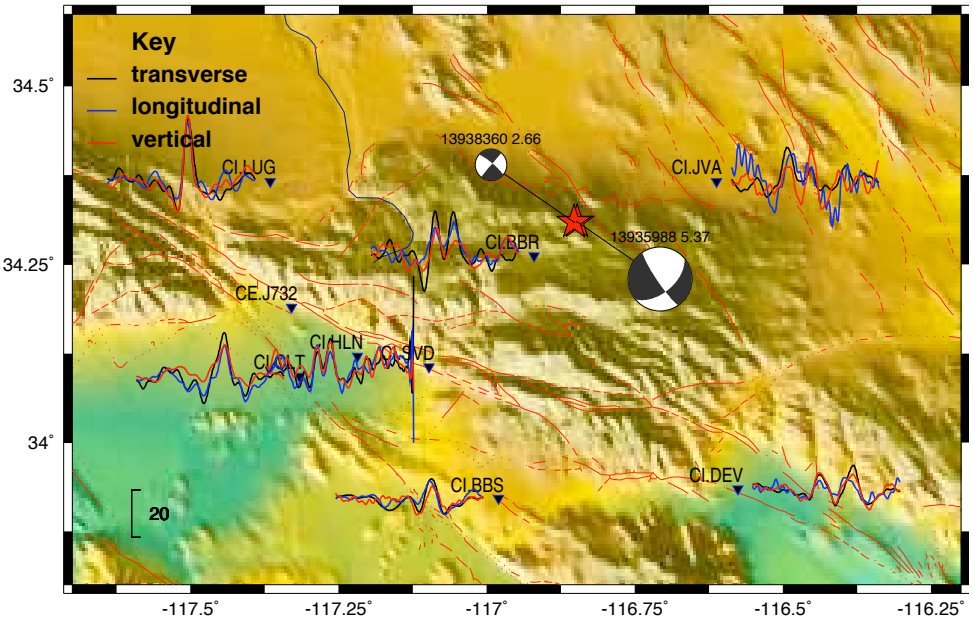

Figure 7.33: Transfer Functions for Big Bear from M2.66 — all components. Each time-series is $4s$ long, with time from $-1s$ to $+3s$.

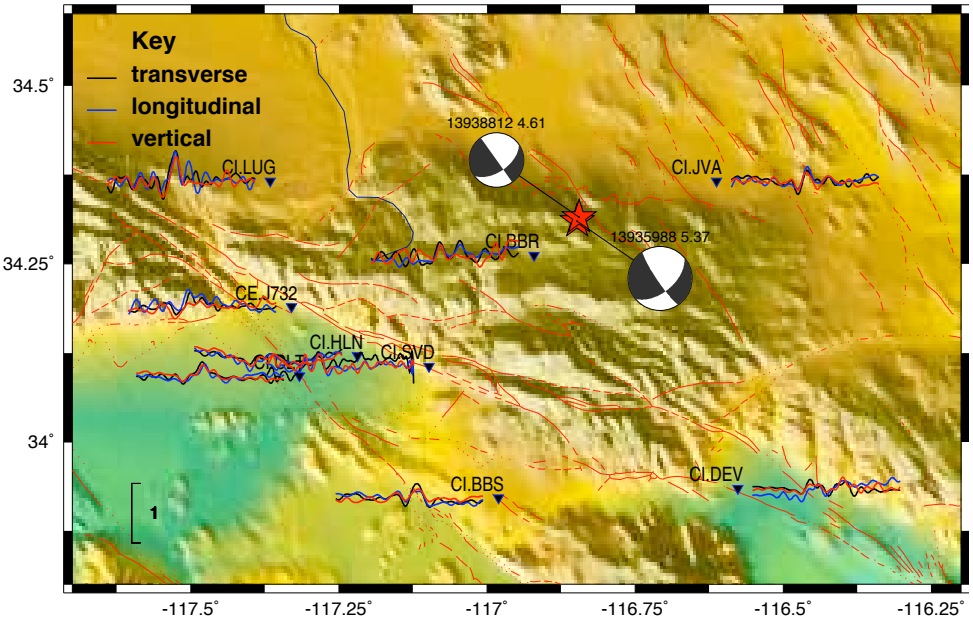

Figure 7.34: Transfer Functions for Big Bear from M4.61 — all components. Each time-series is $4s$ long, with time from $-1s$ to $+3s$.

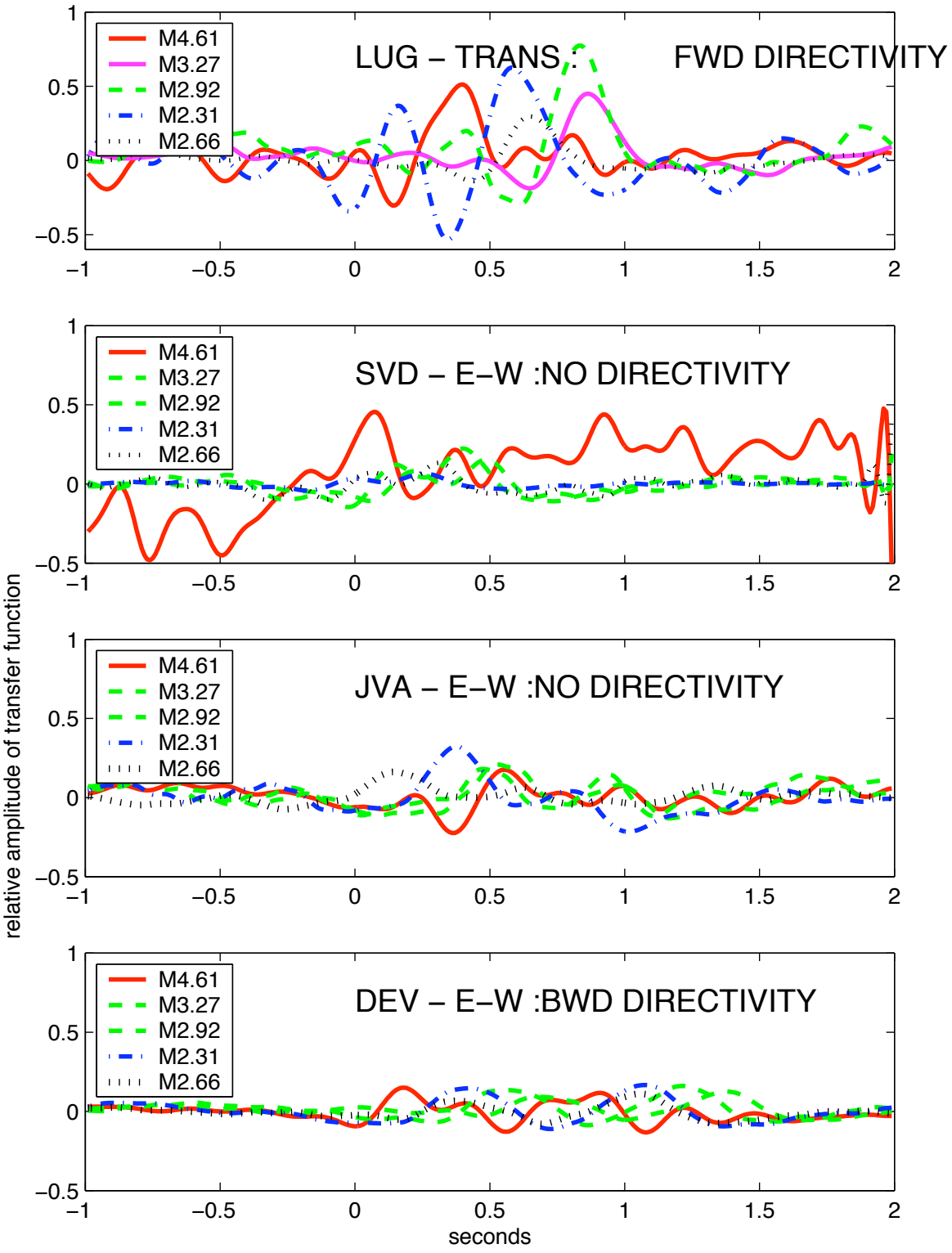

Figure 7.35: Big Bear: individual station source time series comparison. All events are scaled by potency, relative to M4.61 event.

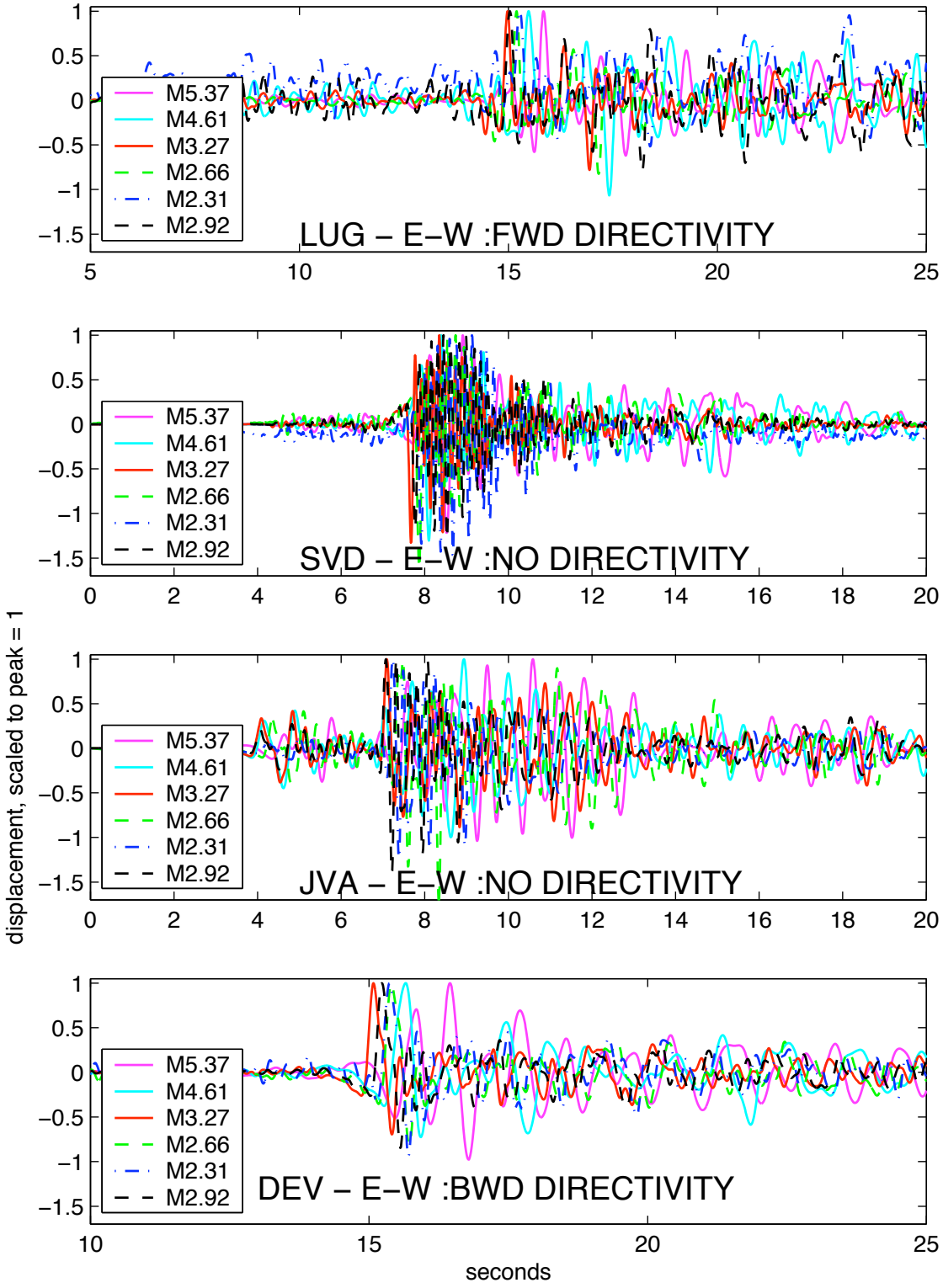

Figure 7.36: Big Bear: individual station timeseries comparison. all timeseries scaled to unit amplitude.

San Jacinto fault zone, a member of the San Andreas fault system, at a depth of 14.5km.

The earthquake focal mechanism exhibited mixed left-lateral strike-slip and thrust motion on a vertical fault striking N35^{o}E. This trend that is orthogonal to the strike of the San Jacinto fault suggests that the earthquake occurred on a restraining bend in the San Jacinto fault zone. Such geometrical complexities (bends) inhibit the movement on the main fault strand that shows strike-slip motion and strikes northwest. The aftershocks also show a northeast trend and mostly occur in the depth range of 13 to 16km, extending over a zone about 4km wide.

Unfortunately few of the aftershocks have similar first motion focal mechanisms and are closely located to the mainshock. An example of one aftershock with a similar focal mechanism is the M_L2.9 at 02:27PST the next day, (31 October 2001), with a depth of 15.2km. Figures 7.37 and 7.38 present the timeseries and source time functions for this aftershock / mainshock. The source time functions do not clearly indicate any directivity. This may be due to a variety of reasons; the mainshock focal mechanism is not as simple as the essentially strike-slip motion for the Yorba Linda event, and so the expected pattern may not be easily recognisable; the mainshock rupture may be bi-lateral; or the aftershock selected may not be a good selection as a Green's function. To further complicate matters, the events occurred in a more sparsely instrumented region, and so less data is available with good signal to noise.

7.4 Conclusions and Discussion

The revolutionary nature of the data that is systematically collected by TriNet allows development of new methodologies for studying the source process. Past source studies of earthquakes in the M4 range have primarily been based on spectral techniques (e.g corner frequencies and the Brune stress drop (Brune, 1970)). Unfortunately, these spectral techniques do not generally consider the particular source-station geometry, nor do they consider the particular effects introduced by complex wave propagation. These complex effects include the interference of multiple phases, diffraction and head waves. While there are still simplifying assumptions in the methodology outlined in this Chapter, this proce-

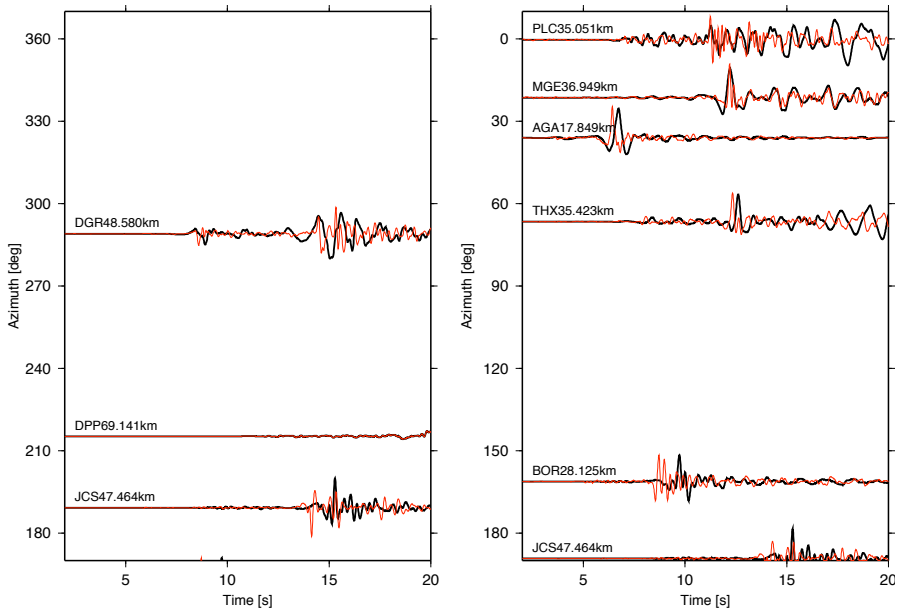

Figure 7.37: Displacement timeseries comparison with M2.90 and Anza mainshock — E-W component.

dure is likely to provide a more meaningful quantification of the source.

Now that the method has been shown to produce source time functions consistent with the expected rupture pattern, the next step would be to invert the source time functions from all the stations to derive the source parameters (fault plane, rupture dimension etc.). Unfortunately, such an inversion is not well enough conditioned to allow a general sub-fault inversion of the type usually employed for larger magnitude earthquakes (e.g Hartzell and Heaton (1983)). Instead, a much simpler parameterisation could be employed. We would begin by assuming one of the conjugate planes derived from the first-motion studies. We then assume that the source consists of a an ellipsoidal patch (2 degrees of freedom), a rupture velocity, and a rise time. This gives a total of 7 degrees of freedom to describe the source. We then would use a neighbourhood algorithm to perform the nonlinear inversion for the 7 parameters that best predict the source time functions. This process would be repeated for the other conjugate fault from the first motion analysis. The conjugate plane that produces the smallest residual would then be chosen as the preferred fault plane. Stress drop would be calculated from the rupture dimensions and the average slip.

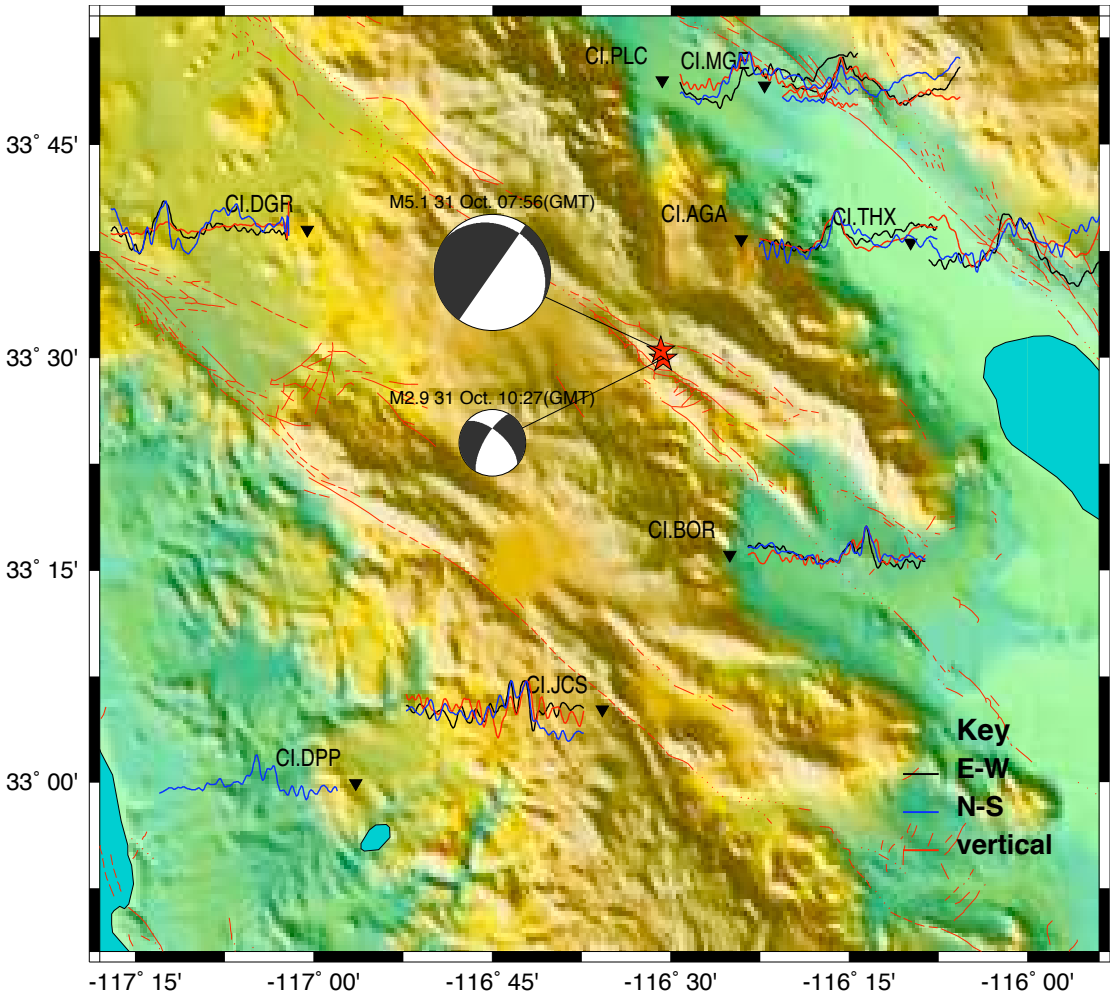

Figure 7.38: Transfer Functions for Anza from M2.90 — all components

As previously mentioned, the underlying assumption of this method is that the Green's function represented by the aftershock is valid for the mainshock. The implications of this for the choice of aftershock have been discussed, but it is this assumption that also places a bound on the application of this method for larger earthquakes. The mainshock to be modelled using an aftershock as a Green's function must possess a simple source time function. In particular it requires that the source-plane is two-dimensional with a constant rake, so that the initial focal-mechanism will be consistent through-out the event. Furthermore, as the rupture length becomes large, the path followed by waves from dislocations far from the epicentre become less similar to the path of the Green's function defined for that epicentre. Large magnitude events which tend to have a complicated rupture pattern over a large length, will likely violate the method's assumptions.

Stress Drop The non-linear inversion of the source time functions which locates the conjugate focal planes on which rupture took place also provides an estimate of the length of the rupture, L, the velocity of rupture, v_r, and a duration for the event, $\Delta T_f = LV_r$.

To calculate the event stress drop, $\Delta\sigma$, we know that:

$$\Delta\sigma = \Delta\varepsilon \cdot \mu \tag{7.36}$$

where $\Delta\varepsilon$ is the strain drop, and μ is the rigidity,

but:

$$\Delta\varepsilon = \frac{\overline{D}}{L} \tag{7.37}$$

where $\overline{D}$ is the average slip over the length of the fault,

also, recall from the definition of seismic moment, M_0, assuming the area is roughly a square with length L:

$$\overline{D} = \frac{M_0}{\mu L^2} \tag{7.38}$$

So we have:

$$\Delta\sigma = \frac{M v_r^3}{T_f^3} \tag{7.39}$$

It is particularly interesting to quantify the variability of stress drop for these smaller

earthquakes. That is, we know that the average stress drop of larger earthquakes is generally less than $10 MPa$. Can we demonstrate that a wider range of stress drops occur for smaller earthquakes? The answer to this question has important consequences for the friction and fracture energy that is used in dynamic rupture models.